journal of the international meteor organization

WGN

51:3
june 2023

ISSN 1016-3115

WGN Vol. 51, No. 3, June 2023, pp. 45 – 68

Administrative

Ongoing Meteor Work

Preliminary results

Front cover photo

Chris Hall captured this multi-bursting fireball while photographing this homestead on 2020 June 19, at $05^{h}43^{m}$ UT) from rural Oklahoma, USA. Image courtesy: Chris Hall.

Writing for WGN

This Journal welcomes papers submitted for publication. All papers are reviewed for scientific content, and edited for English and style. Instructions for authors can be found in WGN **45:1**, 1–5, and at `http://www.imo.net/docs/writingforwgn.pdf` .

Copyright

Legal address

International Meteor Organization, Jozef Mattheessensstraat 60, 2540 Hove, Belgium.

In memoriam: Marc Neijts (1953 – 2023)

Felix Bettonvil[1]

Received 2023 July 10

Sadly, on June 17, 2023, at the age of 70, and after a short period of illness, passed away Marc Neijts. Marc was an avid Dutch meteor enthusiast, both active in his home country and abroad. He participated many times in IMCs.

Marc was interested in many aspects of meteor astronomy and his involvement in all activities produced much good. Radio meteor work had his greatest interest, as he was a radio amateur too, and it was him who brought the Dutch radio amateur- and meteor community together. But next to his radio interests, Marc was also always present at the observing campaigns of the major meteor showers such as the Perseids, Geminids or Leonids. He particularly enjoyed the occasions when Dutch weather did not cooperate and last minute expeditions were to be organized.

Marc was key in organizing projects and activities. He was the one who set up a collaboration with Meteor Burst Communications (MBC), a company aiming at the exploitation of communication via radio meteor reflections in remote areas (at a time long before the mobile telephone network would become widespread). He also organized that the first fiber-coupled intensified video cameras could be used in Dutch meteor astronomy, and he arranged for the first infrasound detector for Dutch amateurs.

Undoubtedly, most visible for many must have been his role in organizing three International Meteor Conferences in the Netherlands. Thanks to him they became a big success.

Marc worked until his retirement as a civil servant for social affairs for local governments. Already in his childhood he showed interest in astronomy and space. For a long time he was a member of the Dutch KNVWS Meteor Section of which he was a board member from 1994 to 2006. And home he built all sorts of meteor equipment.

But Marc was above all a nice person. He enjoyed motivating people and paid lots of attention to the human aspects behind our hobby. Being an open, out-spoken and enthusiastic person, he recognized and openly appreciated others' effort, thereby further stimulating and encouraging. In addition to his contacts with many amateurs, he also maintained warm ties with many professionals.

It was a privilege to have Marc in our midst. The many, many observations and all activities we did together will remain in our memories forever.

We've lost a fine meteor friend.

Figure 1 – Marc during the meteorite search expedition near Hasselt in summer 2019.

[1]Email: bettonvil@strw.leidenuniv.nl

IMO bibcode WGN-513-bettonvil-neijts NASA-ADS bibcode 2023JIMO...51...45B

Ongoing Meteor Work

Daytime fireball on 21 February 2023 above Austria and Slovakia

Lukáš Shrbený[1,2], *Pavel Spurný*[1], *Mike Hankey*[3]

We present description of observation of daytime fireball recorded during the afternoon on 2023 February 21. Atmospheric trajectory and heliocentric orbit were determined on the basis of two instrumental video records. The slope of the atmospheric trajectory to the surface is 11 degrees and the initial velocity is 25.5 km s^{-1}. If any meteorite survived the passage through the atmosphere, it would be very small. The heliocentric orbit is similar to the Daytime epsilon Aquariids.

Received 2023 April 14

1 Observations

On Tuesday, 2023 February 21, we received one report via our Czech web form of sightings of a fast moving fireball visible at approximately 15^h51^m UT that day. We manually checked records of our IP video cameras and identified the fireball (hereafter designated as the EN210223_155012 fireball) between $15^h50^m12^s$ and $15^h50^m19^s$ UT. Unfortunately, due to cloudy weather in the Czech Republic (Figure 1), we have only one record from station Kuchařovice (Figures 1(a), 2). Fortunately, the sky was clear in the area of the fireball, so we asked the administrator of the European video network Allsky7 (Hankey et al., 2020) to check their records. Mike Hankey provided us with footage of the fireball from AMS85 in Vienna (Figures 1(b), 2), which is operated by Ludovic Ferriere.

[1]Astronomical Institute of the Czech Academy of Sciences, Ondřejov, Czech Republic.
[2]Email: lukas.shrbeny@asu.cas.cz
[3]American Meteor Society

IMO bibcode WGN-513-shrbeny-fireball
NASA-ADS bibcode 2023JIMO...51...46S

2 Atmospheric trajectory

A projection of the atmospheric trajectory and camera locations is shown in Figure 1 and a more detailed projection is also shown in Figure 3. The lateral deviations of the measured points along the atmospheric trajectory are shown in Figure 4. The basic parameters of the atmospheric trajectory of the EN21022_155012 fireball are presented in Table 1. The fireball lasted 6.6 s and was observed at heights between 67.2 and 39.4 km. The average slope of its atmospheric trajectory to the surface is 11.2 degrees and the length of the observed trajectory is 143.8 km. The initial velocity was computed by the method described in Borovička et al. (2022) and its value is 25.50 ± 0.19 km s^{-1}.

The body decelerated significantly in the atmosphere. In Figure 5 the observed minus computed length along

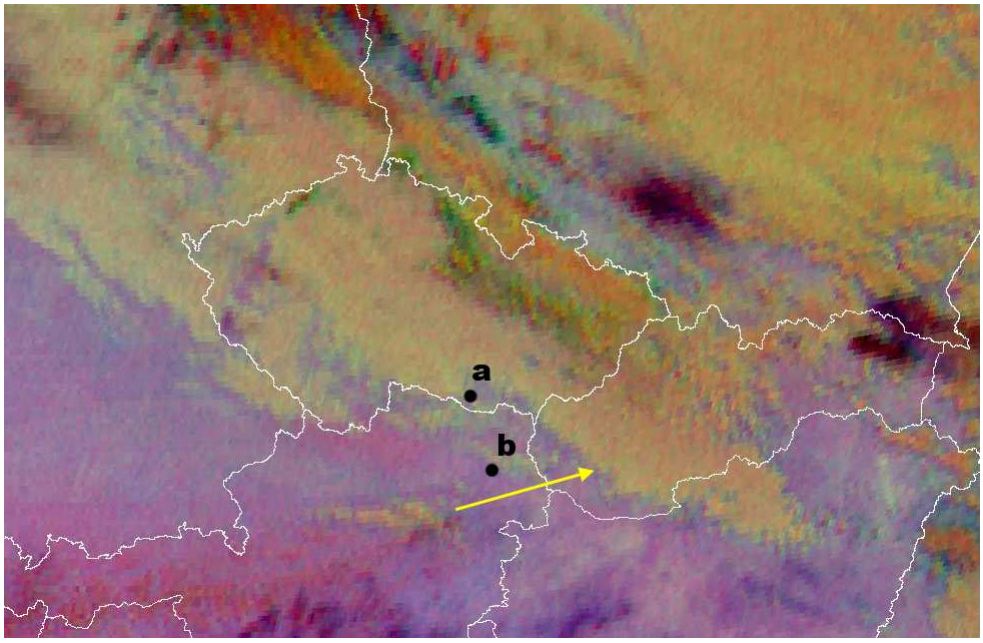

Figure 1 – Satellite image of Central Europe taken on 2023 February 21 at 15^h45^m UT by Meteosat geostationary meteorological satellite (courtesy EUMETSAT and Czech Hydrometeorological Institute). Projection of observed part of the atmospheric trajectory of the fireball (yellow arrow) and locations of the two video camera stations used for the trajectory determination (black dots) Kuchařovice (a), and Vienna (b) are also shown. The meaning of the colours in the picture: red shows vertically massive clouds, dark blue shows sparse cirrus clouds, medium and low clouds are ochre, the lowest clouds and fog are turning green, and pink shows the surface.

Figure 2 – Composition images of the atmospheric trajectory of the EN210223_155012 fireball from Kuchařovice (upper image, AI CAS) and Vienna (lower images, Ludovic Ferriere, AllSky7). The fireball flew from right to left in all images.

the trajectory from physical four-parameter fit to the dynamics data is shown (according to Pecina and Ceplecha, 1983). The velocity at the terminal height of 39.4 km is 14.1 km s^{-1} and the corresponding dynamic mass at this point is approximately 0.4 kg. The meteoroid continued to ablate and its mass continued to decrease. If any meteorite survived the passage through the atmosphere, it would be very small.

The initial mass of 2 kg was determined as a combination of dynamic and photometric mass. The physical four-parameter fit resulted in initial dynamic mass slightly below 2 kg and ablation coefficient of 0.006 s^{2}km^{-2}. The brightness was determined in the same way as for the Antonin daytime fireball (Shrbený et al., 2022) at the Kuchařovice record. The resulting light curve for extinction coefficient of 0.3 provides the photometric mass around 2 kg. The fireball was first detected at the Kuchařovice record having the apparent brightness of −6.5 magnitude and disappeared having the apparent brightness of −7 mag. The maximum brightness was reached at the altitude of 42 km and corresponds to absolute brightness (100 km distance) of −8.6 mag.

From the profile of the light curve it is evident that there were couple of fragmentation events between altitudes of 70 and 50 km. This also is confirmed by the observed length of the wake (Shrbený et al., 2020). The wake was first detected at the altitude of 66 km, which corresponds to the dynamic pressure of 0.09 MPa. The maximum observed length of the wake is 3.7 km at the altitude of 59 km. The wake disappeared at the altitude of 49 km. The maximum dynamic pressure of 0.97 MPa corresponds to the altitude of 41 km.

3 Heliocentric orbit

The geocentric radiant and heliocentric orbit of EN210223_155012 are presented in Table 2. According to the value of the Tisserand parameter with respect to Jupiter of 3.05±0.07, the orbit is on the border between the asteroidal and the orbit of a Jupiter family comet. The orbital elements are similar to one meteor shower from the working list – the Daytime epsilon Aquarids (DEQ, IAU #116). The parameters of the DEQ (Sekanina, 1976) are presented in Table 2. We measured the degree of similarity between the two orbits

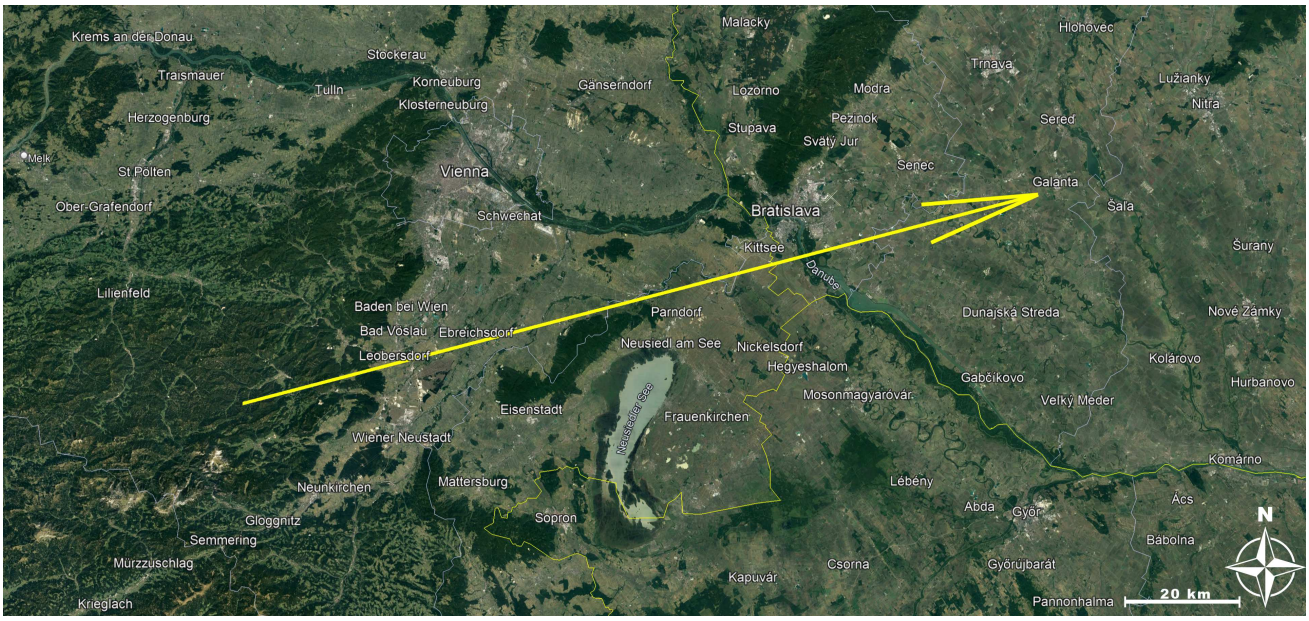

Figure 3 – Projection of the atmospheric trajectory of the EN21022_155012 fireball (Background map: Google Earth).

Table 1 – Parameters of the atmospheric trajectory of the EN210223_155012 fireball as affected by gravity bending.

	h (km)	Long. (°)	Lat. (°)	v (km s^{-1})	z_R (°)	L (km)	p (MPa)	D_K (km)	D_V (km)
beg	67.25	15.87139	47.85238	25.1	78.28	0	0.08	133.5	86.0
end	39.38	17.68537	48.17065	14.1	79.28	143.77	0.92	147.8	105.7

Note: Parameters are given for the observed beginning (beg) and end as follows: h is height, Lat. and Long. are geographical latitude and longitude, v is observed atmospheric velocity, z_R is zenith distance of the radiant, L is length of the trajectory, p is dynamic pressure, D_K and D_V are distances of the fireball from Kuchařovice and Vienna, respectively.

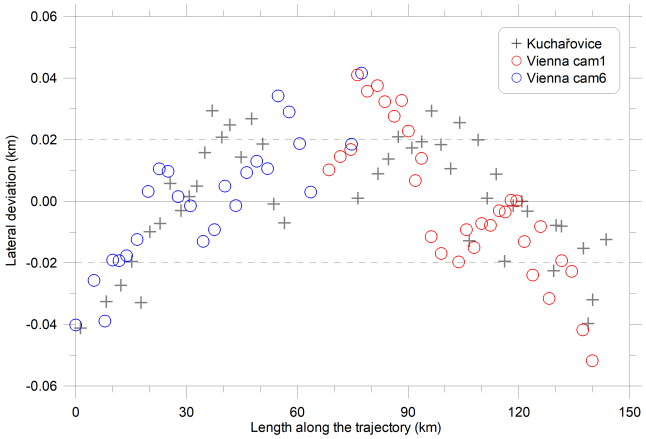

Figure 4 – Lateral deviations of measured points along the atmospheric trajectory. Dashed lines show the range of one standard deviation of 20 m. The curvature of the trajectory due to gravity is visible. Note the different scales on the x- and y-axes.

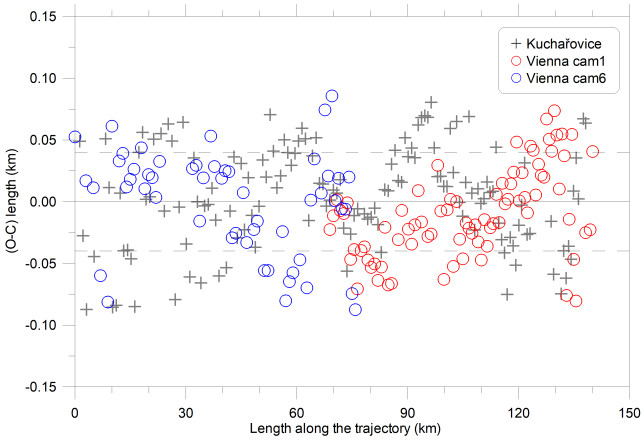

Figure 5 – O-C diagram of the length along the atmospheric trajectory. Solid line corresponds to the physical four-parameter fit to the dynamics data. Dashed lines show the range of one standard deviation of 40 m.

by so called D-criterion. We determined values of D_{SH} (Southworth & Hawkins, 1963) and D_D (Drummond, 1981). The values are presented in the last two rows of Table 2. Based on these D-criteria, the similarity of the orbits is not significant.

Acknowledgements

We would like to thank the witness for his report via our web form on this fireball. This work was supported by the institutional project RVO: 67985815, grant no. 19-26232X from the Czech Science Foundation.

Table 2 – Geocentric radiant and heliocentric orbit of the EN210223_155012 and the Daytime epsilon Aquariid meteor shower (J2000.0).

	EN210223_155012	116 DEQ
Geocentric radiant and velocity		
Right ascension (°)	330.23 ± 0.05	310.9 ± 1.3
Declination (°)	-5.06 ± 0.06	-6.6 ± 1.0
Velocity ($km\,s^{-1}$)	23.28 ± 0.21	23.1 ± 0.3
Heliocentric orbit		
Semimajor axis (AU)	2.37 ± 0.07	2.044
Eccentricity	0.772 ± 0.007	0.741 ± 0.013
Perihelion distance (AU)	0.5406 ± 0.0014	0.529 ± 0.010
Argument of perihelion (°)	87.69 ± 0.14	84.8 ± 1.5
Ascending node (°)	332.4151 ± 0.0002	315.8 ± 1.7
Inclination (°)	5.25 ± 0.07	8.8 ± 0.8
Tisserand parameter	3.05 ± 0.07	
Time of perihelion (day)	2023 Jan 8.33 ± 0.25	
Orbital period (year)	3.66 ± 0.17	2.92
D_{SH}		0.27
D_D		0.09

References

Borovička J., Spurný P., Shrbený L., Štork R., Kotková L., Fuchs J., Keclíková J., et al. (2022). "Data on 824 Fireballs Observed by the Digital Cameras of the European Fireball Network in 2017–2018 I. Description of the Network, Data Analysis, and the Catalog". *Astronomy and Astrophysics*, **667**, A157.

Drummond J. D. (1981). "A test of comet and meteor shower associations". *Icarus*, **45**, 545–553.

Hankey M., Perlerin V., and Meisel D. (2020). "The All-Sky-6 and the Video Meteor Archive System of the AMS Ltd". *Planetary and Space Science*, **190**, 105005.

Pecina P. and Ceplecha Z. (1983). "New aspects in single-body meteor physics". *Bulletin of the Astronomical Institute of Czechoslovakia*, **34**, 102–121.

Sekanina Z. (1976). "Statistical Model of Meteor Streams. IV. A Study of Radio Streams from the Synoptic Year". *Icarus*, **27**, 265–321.

Shrbený L., Krzesińska A. M., Borovička J., Spurný P., Tymiński Z., and Kmieciak K. (2022). "Analysis of the daylight fireball of July 15, 2021, leading to a meteorite fall and find near Antonin, Poland, and a description of the recovered chondrite". *Meteoritics & Planetary Science*, **57**, 2108–2126.

Shrbený L., Spurný P., and Borovička J. (2020). "Fireball fragmentation in the first half of the atmospheric trajectory". *Planetary and Space Science*, **187**, 104956.

Southworth R. B. and Hawkins G. S. (1963). "Statistics of meteor streams". *Smithsonian Contributions to Astrophysics*, **7**, 261–285.

Handling Editor: Javor Kac

Detection of very low Frequency (VLF) Radio Bursts during the Reentry of Hayabusa 2 Sample Return Capsule (2020)

Takashi Watanabe[1]*,Miki Kobayashi*[2]*, Yasuo Katoh*[3]*, Kazuo Shiokawa*[3]*, Hiroyo Ohya*[4]*, Kazuhiro Suzuki*[2]*,Satoshi Tanaka*[5]*, Yoshiaki Ishihara*[6]*, Tetsuya Yamada*[5]*, and Makoto Yoshikawa*[5]

A trial to detect very low frequency (VLF) radio emission was performed upon the reentry of the sample-return capsule (SRC) of Hayabusa-2, which took place on 2020 December 05 (UTC) in Woomera Prohibited Area, South Australia. The observational frequency range was from 100 Hz to 48 kHz. No notable thundercloud activity was reported in the area along the reentering trajectory of the SRC in the sub-ionospheric atmosphere. Weak non-impulsive radio bursts with a duration of 10–20 ms were intermittently detected in the maximum-brightness period of the fireball phase of the reentry. Their radio spectra show characteristics of close-distance origin, e.g., negligible dispersion. Observed time delays between the ground waves and their associated skipped sky waves in the earth-ionosphere space are consistent with those predicted from the estimated location of the reentering SRC. These analyses strongly suggest that the observed VLF radio bursts were generated during the maximum of the fire-ball phase of the SRC around the altitudes of 60 km from the ground. The electric discharge taking place in the highly turbulent plasma environment around the SRC in its fireball phase is suggested to be the origin of observed radio bursts.

Received 2023 May 3

1 Introduction

Keay (1980) suggested the presence of very-low-frequency (VLF) radio emission upon displays of bright meteors (fireballs) or reentries of spacecraft in his discussion on electrophonic phenomena. A trial to detect spacecraft-reentry-associated VLF radio emission in this frequency band was performed by Beech and Murray (2005) during the re-entry of the Sample Return Capsule (SRC) of Genesis, taking place on 2004 September 8 in the Oregon-Nevada area. They reported that no distinctively re-entry-related radio signal was detected. Verveer et al. (2000) reported the presence of geomagnetic-field variations of about 40 nT and associated electrophonic sounds upon the reentry of the MOLNIYA 1-67 took place over Australia on 2000 January 27, but no VLF radio observation was performed. After these pioneering observations, a project was planned to monitor environmental VLF radio signals upon the reentry of the Hayabusa 2 SRC took place at the midnight of 2020 December 5 (UTC) at Woomera Prohibited Area, South Australia. In this work, it will be important to establish reasonable methods to identify SRC-related radio signals in the very dense "bush" of natural radio pulses produced mainly by lightning discharges ("atmosferics" or simply called "sferics"). In our observations, no direct measurement to estimate the location of the radio source was performed due to practical limitations. To separate reentry-associated radio signals from normal sferics, we will employ well-known procedures to analyze VLF records of sferics (e.g. Bianchi and Meloni, 2007), based on observed waveforms and frequency spectra. In this report, initial outcomes of the analysis and provisional discussions on the origin of the low-frequency radio signals upon the reentry of the SRC will be given also.

2 Observation

Radio observation of VLF radio waves in the range covering from 100 Hz to 48 kHz was performed at a tracking post of the reentry in the Woomera Prohibited Area, South Australia. A single wide-band loop antenna (500-turn, 50 cm in diameter) was used in our observation. The gain of the observational system including the loop antenna and the amplifier was set to be flat in the frequency band. The radio signal was recorded by a digital audio recorder (TASCAM DR-70D) by a sampling rate of 48 kHz. We also recorded time markers (seconds and minutes) produced from the GPS signal. A set of built-in stereophonic microphones of the recorder was employed to monitor environmental sound. The whole observational system was run under the Japan Standard Time (JST, UTC+9:00). The time difference between the JST and the Australian Central Standard Time (ACST, UTC+9:30) is −0.5 hours. In this report, the JST will be used mainly to avoid confusion in data handling.

A set of examples of the waveform and the dynamic spectrograph of environmental radio noise is shown in Figure 1 covering the frequency band from about 0.1 to 24 kHz (half of the sampling rate) in the time interval from $02^{h}28^{m}45^{s}$ to $02^{h}29^{m}30^{s}$ on 2020 December 06 (JST), including the principal portion of the nominal fireball phase of the re-entering SRC in the interval from $02^{h}28^{m}48^{s}$ to $02^{h}29^{m}22^{s}$ (JST). Sferics appear

[1]National Institute of Information and Communications Technology, Koganei, Tokyo 184-8795, Japan. Email: watanabeggl@gmail.com

[2]Nippon Meteor Society, https://www.web-nms.com/

[3]Institute for Space-Earth Environmental Research, Nagoya University, 464-8601 Nagoya, Japan.

[4]Graduate School of Engineering, Chiba University, Chiba 263-8522. Japan.

[5]Institute of Space and Astronautical Science, Japan Aerospace Exploration Agency, Sagamihara 252-5210, Japan.

[6]JAXA Space Exploration Center, Japan Aerospace Exploration Agency, Sagamihara 252-5210, Japan.

IMO bibcode WGN-513-watanabe-vlf
NASA-ADS bibcode 2023JIMO...51...50W

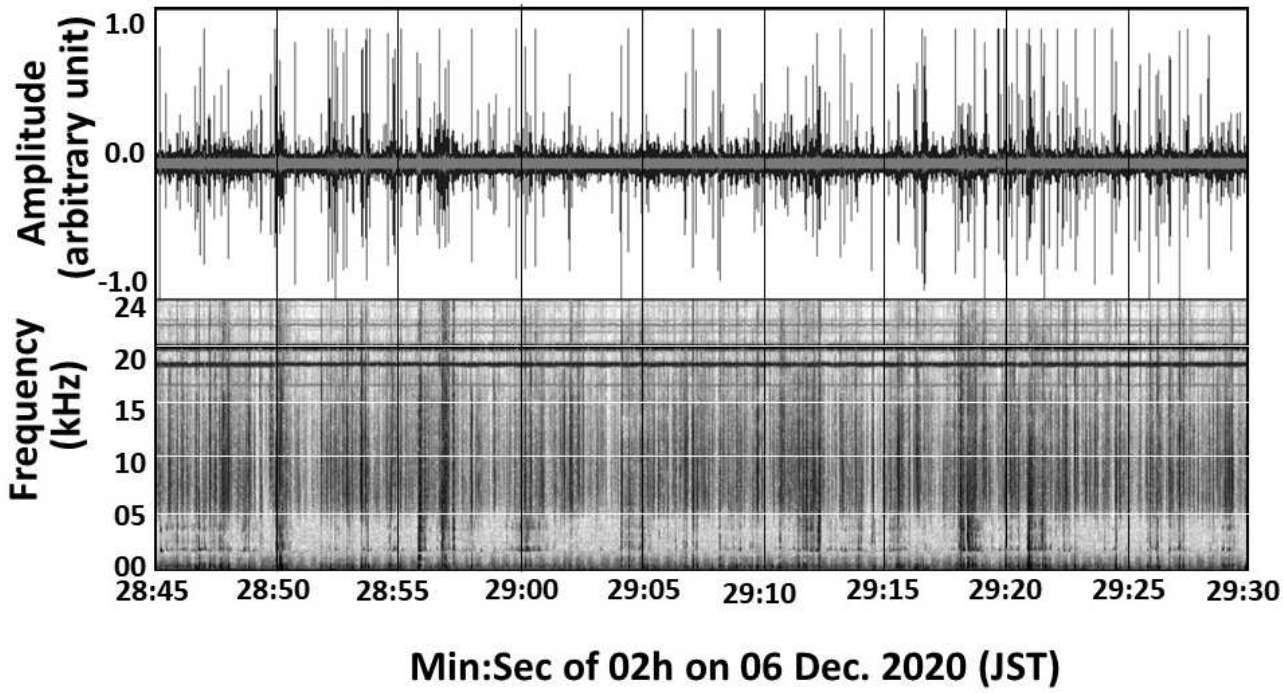

Figure 1 – A set of examples of the waveform (the time variation of amplitude) and the dynamic spectrograph (darker patterns are stronger emissions) of environmental VLF radio noise observed at the monitoring site of the reentry of Hayabusa-2 Sample Return Capsule, during the interval from $02^{h}28^{m}45^{s}$ to $02^{h}29^{m}30^{s}$ on 2020 December 6 (JST, UTC+9:00). This interval covers entire fireball phase of the SRC, reaching its maximum at about $02^{h}29^{m}00^{s}$ (JST). The dynamic spectrogram covers the frequency band from about 100 Hz to 24 kHz. Several horizontal lines seen in the frequency range higher than 17 kHz is produced by global VLF stations for navigational aid. The majority of impulsive patterns were sferics generated by thundercloud activities.

in the spectrogram as narrow vertical patterns with a variety of frequency coverage. Several horizontal lines seen in the frequency band higher than 17 kHz are produced by global VLF stations for navigational aid. The strongest signal came from the NWC (19.8 kHz) on the west coast of Australia. These interferences are filtered out in detailed analysis to reduce the background noise level.

To grasp the general situation of sferics being observed during the reentry of the SRC, propagation distances of relatively strong sferics are estimated by measurements of their slow-tail patterns in the waveforms, appearing in the frequency region below 300 Hz (Mackay & Fraser-Smith, 2010). The majority of recorded spferics originated at distances of >500 km from the observational site during the reentry of SRC. According to international weather-satellite cloud images and local weather maps, a weak weather front, located at about 500–1000 km to the north of the observational site, and several tropical and subtropical storms were identified around the Australian continent. These meteorological structures are presumed to have been the principal sources of observed sferics. According to a whole-sky image of the trajectory of reentering SRC (Tanno et al., 2022), the sky around the trajectory was generally clear during the fireball phase. The site of radio observation was covered partly by scattered clouds, as thin as the moon was visible through the clouds. These available weather information showed that notable thundercloud activities were absent at least in the circle with a radius of 500 km centered at the observational site during re-entry of the SRC.

3 Spectral Analysis

As stated in the previous section, the majority of recorded radio signals in the VLF radio band are thundercloud-originated sferics. In this research, it is crucial to establish procedures to separate the SRC-related signals from sferics being recorded at a rate of nearly one hundred per second. The spectral analysis will be useful as the initial step to find radio signals of close-distance origin because the distance between the observational site and the SRC during the fireball phase of the SRC was 60–200 km. Figure 2 shows an example of a high-resolution (Wavelet) dynamic spectrum with a time resolution of 12.7 msec at 1 kHz, covering the interval of 300 ms (starting at $02^{h}58^{m}57^{s}.9$ on 2020 December 06, JST) in the fireball phase of the SRC. Radio signals seen in the dynamic spectrum can be categorized into three types (A, B, and C) based on the characteristics of the waveforms and the spectra in the frequency domain (FFT). They are respectively shown in the upper and the lower panels below the dynamic spectrum. Brief descriptions of these categories are given below respectively:

A) (Tweek-type sferic): In the dynamic spectrum, relatively strong sferic of this type shows an almost vertical line with a duration of several milliseconds at the frequency area higher than 2 kHz

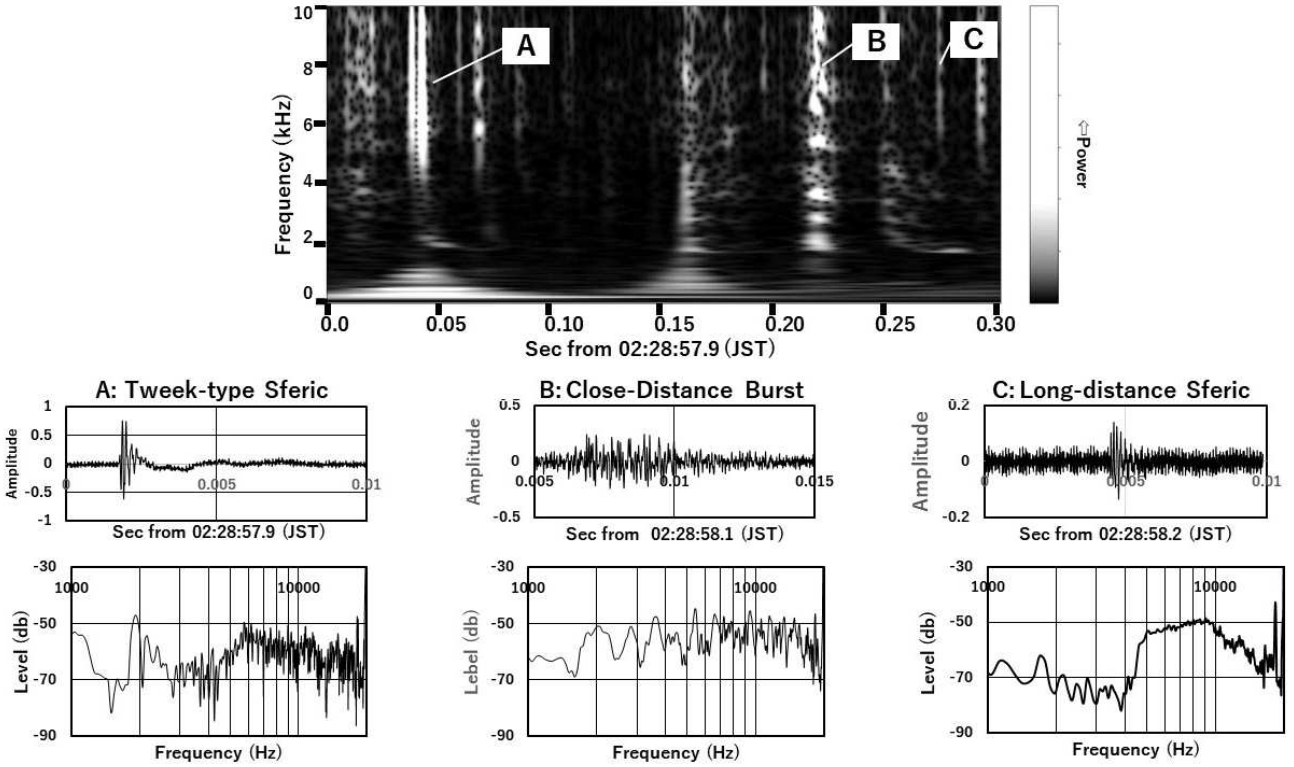

Figure 2 – Characteristics of three kinds of VLF radio signals observed during the reentry of the Hayabusa-2 Sample Return Capsule taking place on 2020 December 6 (JST). Top panel: The dynamic spectrum for the time interval of 300 ms starting at $02^{h}28^{m}57^{s}.6$ on 2020 December 6 (JST). Three selected signals are indicated as A (tweek-type sferic), B (close-distance burst), and C (long-distance sferic), respectively. The waveform and frequency spectrum of these three examples are respectively shown in the upper and the lower panels below the dynamic spectrum.

and a curved "hook" and a "tail" at the lowest frequencies approaching an asymptotic frequency (cut-off frequency, Fc, of the earth-ionosphere waveguide). The Fc at the time of observation is estimated to be about 1.7 kHz. The hook and the tail are produced by the dispersive nature of the waveguide around Fc (Weit, 1964). The propagation distance of the tweek can be estimated from the geometry of the hook-tail pattern (Yano et al., 1989). In this particular case, the propagating distance is estimated to be about 1500 km. A broad depression of spectral power in the frequency region of 1–5 kHz is generated by the attenuation of the waveguide (e.g., Barr et al., 2000).

B) (Close-distance radio burst): This is a white-noise-like radio burst to endure 10–15 milliseconds and has a largely flat spectrum. Negligible attenuation in the frequency region of 1–5 kHz and no appreciable dispersive characteristics suggest its close-distance origin. Radio bursts of this type will be candidates for re-entry-related VLF radio signals.

C) (Long-distance sferic): Relatively weak sferic of this type is generated by long-distance (>1000 km) thundercloud activity. Strong depression of the spectral power in the frequency region of 1–5 kHz is produced by attenuation of the ground-ionosphere waveguide. A broad peak of the spectral power is seen around 8–10 kHz. The waveform shows simple quasi-sinusoidal characteristics.

After detailed analyses of waveforms and spectra of radio signals observed during the interval of several tens of minutes centered at the nominal fire-ball phase of the SRC (from $02^{h}28^{m}48^{s}$ to $02^{h}29^{m}22^{s}$, JST), candidates of reentry-related radio bursts generated at the distances of reentering SRC were selected based on criteria mentioned above. About 10 examples of close-distance without appreciable overlapped background sferics were found mainly in the interval around the timing of the maximum of the SRC's fireball phase. Since no notable thundercloud activity was reported in the area around the trajectory of the reentry of SRC, these close-distance radio bursts are suggested to have a close connection with the reentry of SRC. However, it is impossible at present to estimate distances closer than 500 km owing to the limitation in the time resolution of current techniques of spectral analysis. In addition, there still exists a possibility that observed close-distance radio bursts were generated by unrecorded atmospheric phenomena took place near the observational site. In the next section, a procedure to overcome these limitations of spectral analysis will be given.

4 Ray-hop Analysis

The fundamental difference between thunderclouds and the reentering SRC is in their altitudes from the ground. The majority of the lightning discharges are

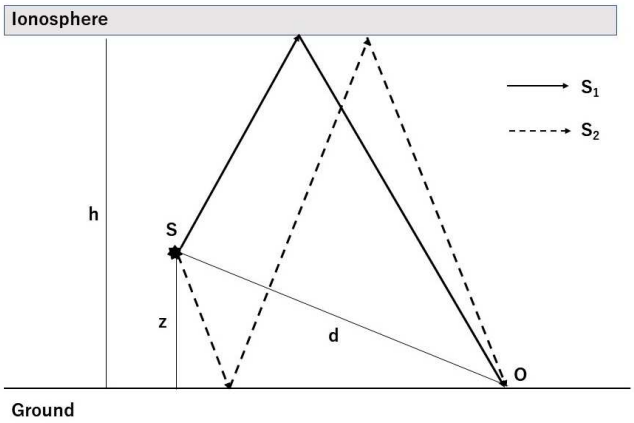

Figure 3 – The geometry of skipped waves in the ground-ionosphere space with the height of h. The location of the radio source with the height of z and the observational point on the ground are indicated by S and O, respectively. The horizontal distance between S and O (the pass length of the ground wave) is d. Case S_1 (thick folded arrow) involves a one-time reflection at the ionosphere to reach O. Case S_2 (broken folded arrow) involves a one-time reflection at the ground surface and the subsequent reflection at the ionosphere.

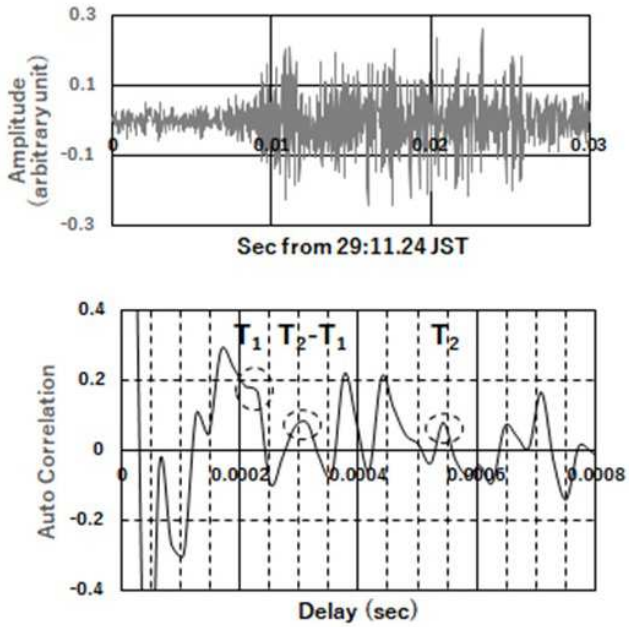

Figure 4 – The auto-correlation analysis of the waveform of the VLF radio burst took place at $02^{\rm h}29^{\rm m}11^{\rm s}$ on 2020 December 6 (JST). Upper panel: The original waveform. Lower panel: Auto-correlogram of the waveform shown in the upper panel. Three kinds of delays of sky waves formed in the ground-ionosphere space are indicated by T_1, T_2, and $T2 - T1$ respectively (see text).

taking place in the low troposphere, mainly below 6 km from the ground. On the other hand, the altitudes of the SRC ranged between 40 and 100 km during its fireball phase (Yamada & Yoshihara, 2022). It is known that the observed waveform in the VLF frequencies consists of the directly received wave (ground wave) and skipped waves (sky waves) in the ground-ionosphere cavity. Owing to their long-distance propagations, sky waves are observed with delays after the detection of the ground wave (Tayler, 1969). In the case of reentering SRC, the location in the ground-ionosphere space at a given time (the height from the ground and the distance from the observational site) is known, and expected delays can be estimated by assuming the height of the reflection layer in the ionosphere. By checking the consistency between the predicted and the observed delays in the waveform, we can identify the observed radio signal radiated at the position of the reentering SRC.

As shown in Figure 3, two kinds of sky waves are formed in the ground-ionosphere space. The first case (S_1 in this figure) involves one-time ionospheric reflection with the delay of T_1. The second one (S_2) involves the initial reflection by the ground surface and the subsequent ionospheric reflection with the total delay of T_2. The time difference between these delays ($T_2 - T_1$) is useful because the ambiguity in the height of the reflection point in the ionosphere can be eliminated considerably. The ray-hop analysis has been employed by many authors to estimate the location of an impulsive lightning discharge whose waveform shows clear repeating patterns produced by ray hops. On the other hand, in cases of radio bursts observed upon the re-entry of SRC, it is impossible to identify individual combinations of the ground wave and associated sky waves because the waveform of the radio burst consists of numerous ground waves and their sky waves. To overcome this difficulty, the auto-correlation analysis is performed to find the correlated time delays corresponding to the location of the SRC. An example of the correlogram for the case of close-distance radio bursts observed shortly after the maximum of the fireball phase at around $02^{\rm h}29^{\rm m}11^{\rm s}$ (JST) is shown in Figure 4. The height of the reflection point is estimated to be about 90 km from the ground, based on the value of observed Fc (1.7 kHz). In this example, significant coincidences between each of the predicted and estimated delays are seen within the ambiguity of the reflection height. The correlogram also shows several extra correlations. Those with larger delays are produced partly by multiple reflected waves. Quasi-periodic occurrences of pulses will be another possibility to create extra correlations having no relationship with reflections in the ground-ionosphere space.

Among candidates for the reentry-associated radio signal, six radio bursts showed significant consistency between predicted and observed delays for all three kinds of delays. The timings of their detections are shown in Figure 5 in the diagram of time variation of the visual and the absolute magnitudes of SRC in the fireball phase, estimated from video records taken at a separate station near the trajectory. Although the ray-hop analysis cannot be applied in the early stage of the fireball phase, owing to too short delays to be measured with our data-sampling rate (48000/second), the SRC-related radio bursts tend to be nested around the peak of the fireball phase of the reentering SRC at the altitude of about 60 km. There exists another tendency that the radio bursts were observed in association with sporadic brightening of the SRC.

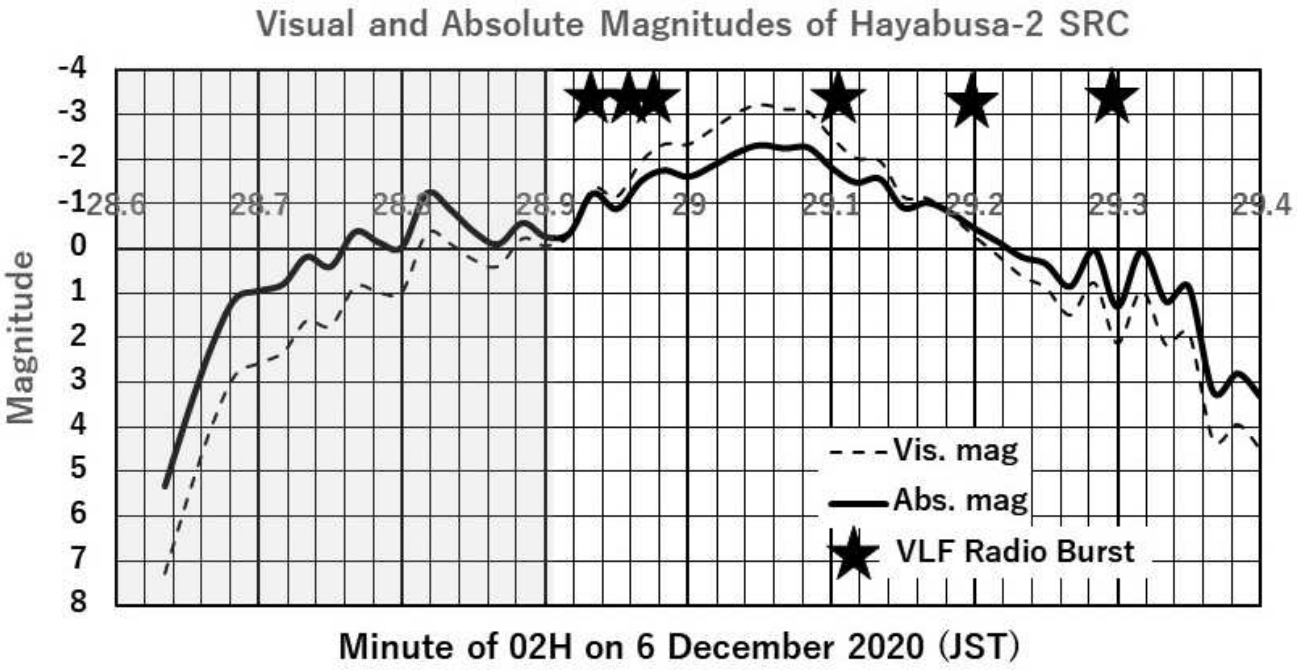

Figure 5 – Time variations of the reentering Hayabusa-2 Sample Return Capsule and the occurrence instances of close-distance VLF radio bursts having close connections with the re-entry. The time axis is represented by the decimal minutes starting at $02^{\mathrm{h}}28\overset{\mathrm{m}}{.}6$ on 2020 December 6 (JST). The visual magnitude (broken line) is converted to the absolute magnitude at 100 km from the observational site. The atmospheric attenuation is corrected. Asterisks indicate the timings of detections of VLF radio bursts suggested to have close connections to the reentry (see text). In the shaded time interval, the ray-hop analysis (see text) cannot be applied because the shortest delay (T_1) is under technical limitation (about 40 microseconds).

5 Discussion

In this stage, only a limited discussion on the generation mechanism of observed VLF radio signals can be made owing to the scarcity of information on the physical conditions of the SRC upon its reentry. Concerning VLF radio observation, the electric field strength of the observed radio signal is only one parameter to be employed in the current discussion. The typical electric field strength of the radio bursts was measured to be about 10^{-3} V/m per 1 kHz bandwidth, almost equivalent to those of stepped leaders of lightning discharges (Heavner et al., 2002). A measure of the electric current, which is required to produce the radio emission of this level at the distance of the SRC from the observational site (about 170 km at the time of data acquisition), can be estimated by the fundamental antenna theory (e.g. Wright, 1987) by assuming a virtual rod antenna. The high-temperature and high-density halo and the trail of ionized abraded gas formed around the SRC will be a candidate for the source of VLF radio emission because a strong electronic field will be formed by the diffusive charge separation of ions and electrons. However, according to aerodynamic modeling of the environment of the halo (Yamada & Abe, 2006), the characteristic diameter of the high-density plasma envelope (the halo) of the SRC is only 1 meter. In this case, the required electric current to produce the observed VLF signal is on the order of 10^3 A enduring 10–20 ms because the emissivity is directly proportional to the ratio of antenna length/wavelength. It will be unlikely to imagine that such a very strong electric current in the VLF bunds with a wavelength of several tens of kilometers was formed in such a small-scale halo of the SRC. On the other hand, a more plausible place to realize the longer electric current will be the ionized wake of the SRC. The SRC was moving with speeds of about 10 km/s, much higher than the thermal speeds of ions (1–2 km/s at 10^4 K). Owing to the presence of the geomagnetic field, electrons tend to be left behind and ions will stay around the SRC. The charge separation will be neutralized quickly by displacement of ions and electrons (namely by the electric current) and the electromagnetic wave covering a broad frequency band will be emitted. A similar process was proposed by Kelley and Price (2017) in their discussion on electromagnetic processes relating the VLF radio emission upon the display of very bright meteors (fireballs). In cases of VLF radio bursts showing the connection with the reentry of the SRC, the typical duration of the radio bursts is about 10 ms. In this time interval, the SRC traveled about 100 m. If we take this value as the upper limit of the length of the virtual rod antenna, the estimated electric current to be applied to the antenna is about 30 A, almost equivalent to those of stepped leaders of thunderclouds with a typical duration of 20 ms (Uman, 1987). Detailed discussions will be necessary based on more detailed physical parameters in the halo and trail of the SRC.

6 Concluding Remarks

The principal objective of this report is to show the presence of VLF radio signals apparently relating to the re-entry of a spacecraft, HY2 SRC, taking place on 2020 December 05 (UT) in South Australia. After detailed analysis of low-noise records of radio signals in the frequency band of 100 Hz – 24 kHz, several examples of weak radio bursts with durations of 10 – 20 ms were found during the fireball phase of the reentering SRC taking place at the altitude of 60–100 km in the sub-ionospheric area. These radio bursts showed spectral characteristics of close origin, e.g. no appreciable evidence of dispersion around the cut-off frequency (about 1.7 kHz) of the earth-ionosphere waveguide. The skip-wave analysis of the waveforms of these signals showed consistency with predicted delays based on the directly estimated locations of the SRC. In addition, no appreciable thundercloud activities were reported in the area around the observational site of <500 km. Although the direct measurements of locations of the sources of the radio bursts were not performed, it will be reasonable to conclude that VLF radio bursts of a measurable level were generated during the reentry of the HY2 SRC in its fireball phase.

Data-analysis procedures employed in the present work can be applied to the future study of meteoric VLF radio emission to avoid confusion with thundercloud-originated spherics. In future VLF radio observations of reentering spacecraft (as well as meteoric fireballs), introducing a location-finding technique will be important. Concerning the generating mechanism of the radio bursts, electric discharges will be the most plausible mechanism owing to the white-noise-like nature of their frequency spectra. Further discussions are needed based on measured and predicted parameters of the plasma environment of the reentering SRC and its trail.

Acknowledgements

The collaboration of JAXA's Hayabusa-2 SRC recovery team would be highly acknowledged because the VLF observation in Australia was performed by the staff of the team owing to COVID-19 travel constraints. We would thank Mr. T. Kumamori of the ALPO-Japan for provided us with the luminance measurement software. We would acknowledge Mr. K. Saito of the Miyagi Prefectural Reimei High School who kindly inform us weather conditions recorded at the observational site. We would thank Mr. K. Wang of the Australian Bureau of Meteorology's Space Weather Services for providing us with ionospheric data in Australia at the time of the reentry of the SRC. This research is supported by the Joint Research Program of the Institute of Space-Earth Environmental Research, Nagoya University.

References

Barr R., Jones D. L., and Rodger C. J. (2000). "ELF and VLF radio waves". *Journal of Atmospheric and Solar-Terrestrial Physics*, **62**, 1689–1718.

Beech M. and Murray I. (2005). "VLF monitoring of the Genesis Sample Return Capsule re-entry". *WGN, Journal of the International Meteor Organization*, **33:2**, 59–62.

Bianchi C. and Meloni A. (2007). "Natural and man-made terrestrial electromagnetic noise: an outlook". *Annals of Geophysics*, **50:3**, 435–445.

Heavner M. J., David A. S., Abram R. J., and Ricki J. S. (2002). "LF/VLF and VHF lightning fast-stepped leader observations". *Journal of Geophysical Research*, **107:D24**, 4791–4795.

Keay C. S. L. (1980). "Anomalous sounds from the entry of meteor fireballs". *Science*, **210**, 11–15.

Kelley M. C. and Price C. (2017). "On the electrophonic generation of audio frequency sound by meteors". *Geophysical Research Letters*, **44**, 2987–2990.

Mackay C. and Fraser-Smith A. C. (2010). "Lightning location using the slow tails of sferics". *Radio Science*, **45:RS5010**, 1–10.

Tanno H., Yamada T., Dantowitz R., Hoover Z., Lockwood C., Klemm C., Scott C., Conn R., Nowicki M., Inmann J., Scriven G., Brown C., and Grinstead J. (2022). "Analysis of Surface Temperature of Hayabusa 1 & 2 SRC in Airborne Spectroscopy Measurement". *AIAA AVIATION 2022 Forum*. https://arc.aiaa.org/doi/abs/10.2514/6.2022-3733.

Tayler W. L. (1969). "Determining lightning stroke height from ionospheric components of atmospheric waveforms". *Journal of Atmospheric and Terrestrial Physics*, **31:7**, 983–990.

Uman M. A. (1987). *The Lightning Discharge*. Academic Press, Orlando.

Verveer A., Bland P. A., and Bevan A. W. R. (2000). "Elecrophonic Sounds from the Reentry of the MOLNIYA 1-67 Satellite over Australia: Confirmation of the electromagnetic Link". *Meteoritics and Planetary Science Supplement*, **35**, A163.

Weit J. R. (1964). *Electromagnetic Waves in Stratified Media*. Pergamon Press, Oxford.

Wright H. C. (1987). *An Introduction to Antenna Theory*. Bernard Babani (publishing) LTD, London.

Yamada T. and Abe T. (2006). "Plasma and the Flight Environment of the HAYABUSA Reentry Capsule". *Journal of Plasma Fusion Research*, **82:6**, 368–374.

Yamada T. and Yoshihara K. (2022). "Best Estimated Trajectory and Attitude Motion of Hayabusa2 SRC Reentry Flight". *AIAA Aviation 2022*. https://arc.aiaa.org/doi/10.2514/6.2022-3801.

Yano S., Ogawa T., and Hagino H. (1989). "Waveform analysis of tweek atmosphercs". *Research Letters on Atmospheric Electricity*, **9**, 31–42.

Handling Editor: Javor Kac

Must points to note when working with IAUMDC Shower Database (SD)

Masahiro Koseki[1]

IAUMDC Shower Database (SD) has undergone major reform in recent years. This paper explains the main points of the reform and presents the remaining challenges. I picked up an example where two groups are treated as one in the sense of calling attention to the reader: theta-Pyxidids (#0340 TPY), September Lyncids (#0081 SLY), Microscopiids (#0370 MIC) / Southern June Aquilids (#0165 SZC), and phi-Piscids (#0372 PPS). The MDC does not have a function to check errors in registration applications, and applicants and reviewers need to be careful to avoid such errors.

Received 2023 May 23

1 Introduction

I have been participating in the Working Group (WG) of IAUMDC for several years and published problems of the Shower Database (SD) in WGN (Koseki, 2016). I think it is necessary to describe the outline of the reforms so far and the remaining problems. It would be appropriate to explain by comparing the two versions of the SD (2018 January 13 and 2023 March 29). The abbreviations used in the SD are shown below.

- s: shower status flags
  - * −2: lack, wrong or problems with references
  - * −1: to be removed from the list of established showers
  - * 0: single shower, working list
  - * 1: single established shower
  - * 2: to be established shower
- LoS: averaged ecliptic longitude of the Sun at the shower activity, (J2000, deg),
- Ra: right ascension of the shower radiant (J2000, deg),
- De: declination of the shower radiant (J2000, deg),
- Vg: geocentric velocity (km/s),
- LoR: ecliptic longitude of the shower radiant (J2000, deg),
- S_LoR: Sun centered ecliptic longitude of the shower radiant (deg),
- LaR: ecliptic latitude of the radiant (J2000, deg),
- OTe: observation technique: C–CCD, P–photo, R–radar, T–TV, V–visual.

We express each entry by IAUNo.+Code+Ad.No., 0001CAP00 for the first entry of Capricornids for example hereafter.

2 Big changes in the SD

What was changed and how is detailed in Hajduková et al. (2023). Here are three examples that may be important and useful for readers.

2.1 Removing typographic errors #0005SDA03

I pointed out "The right ascension and the node are in error and should be read 333.7 and 305.6 respectively based on the original paper (`http://adsabs.harvard.edu/abs/1973NASSP.319..183C`, Cook (1973))." (Koseki, 2016). Table 1 compares the entry of #0005SDA03 between the 2018 version (upper) and the 2023 version (lower). Corrections have been made and equinox conversions (B1950.0 to J2000.0) have also been made.

Table 1 – An example of typographic correction.

CODE	Ra	De	Vg	node
0005SDA03	305.7	−16.1	41.4	152.8
0005SDA03	333.78	−16.38	41.4	305.71

2.2 Streams removed from the Working list

If the publication does not reach the MDC on time (within 6 months of the submission date), the stream codes, names, and parameters are permanently removed from the database (Hajduková et al., 2023). Here are two major examples of what has been removed (Table 2). Many of those based on these documents have been deleted, and the supplementary numbers (Ad.No.) have been deleted for them, so they are missing numbers.

2.3 New submission rules

Following is the quote from Hajduková et al. (2023), "New meteor showers sent to the MDC are given a provisional designation only (not a name). The provisional designations are based on the date of submission and are assigned by the MDC according to a rule that involves. As many of you may already be aware of, it is

[1]The Nippon Meteor Society, 4-3-5 Annaka Annaka-shi, Gunma-ken, 379-0116, Japan. Email: `geh04301@nifty.ne.jp`

IMO bibcode WGN-513-koseki-iaumdc
NASA-ADS bibcode 2023JIMO...51...56K

Table 2 – Examples removed from the Working list.

CODE	Ra	De	Vg	References
0001CAP09	303.8	−9.8	22.9	10 Jenniskens et al., 2017 sub to Icarus
0929TXC00	17.24	1.06	62.84	1) Amaral et al., 2018, WGN to be sub.

Table 3 – Newly registered examples to the SD.

CODE	s	Ra	De	Vg	LoS	S_LoR	LaR	References
M2022-Q2	0	342.4	44.0	53.3	113.7	252.69	46.37	1) Greaves, 2022
M2023-D1	0	218.8	28.2	58.9	282.66	282.23	40.78	1) Segon et al. 2023, submitted to eMetN
M2023-D2	0	235.2	60.7	32.8	296.3	248.16	73.73	1) Segon et al. 2023, submitted to eMetN

important to note that the traditional three-letter code and the shower name will not be given immediately; in detail see Jopek et al. (2023)." Table 3 shows the newly reported showers to the SD. For example, M2022-Q2 was the second shower submitted to MDC in the latter half of August 2022. (Jopek et al., 2023)

3 Remaining problems

There are minor problems with the SD, such as inconsistent descriptions and changes in additional numbers (Ad.No.), but there is still a big problem of misidentifications of meteor showers. At the time the prototype of SD was announced, video observation was not well developed and there was not enough data to make proper classifications. There are quite a few meteor showers in SD that don't seem to exist, and there are also quite a few that contain different showers within one shower, and one shower that is disassembled into two showers. The following examples are representative and may be of interest to the reader.

3.1 theta-Pyxidids

There are three entries of #0340 TPY in the SD as shown in Table 4. The first report of TPY was of SonotaCo net (2009) and Jenniskens et al. classified their observations as TPY later. But their identification is clearly a mistake. The radiant distribution drawn by using SonotaCo net 2007–2021 data clearly shows two different activities (Figure 1a). Two concentrations on the inner circle are two TPY activities; the lower one is TPY00 and the upper concentration is TPY01/02.

If we count the radiant number within the inner circle, the result shows two peaks given in Figure 1b (line Nr<=3); DR3, DR10, and DR15 are the radiant density ratios (Koseki, 2019). These peaks coincide with the listed LoS (averaged ecliptic longitude of the Sun at the shower activity) of TPY00 and TPY01/02. Figures 2a and 2b are redrawn activity profiles of TPY00 and TPY02 by counting the radiant number around each exact position shown in Table 4. TPY00 has a sharp peak around $\lambda_\odot = 250°$ and TPY02 has a rather broad peak around $\lambda_\odot = 265°$; these peaks coincide with Table 4.

It becomes clear that TPY01/02 should be given another proper IAUNo. and IAU code. If this would be done, these two activities, that is, shown in Figures 2a and 2b could be ranked as established showers.

a.)

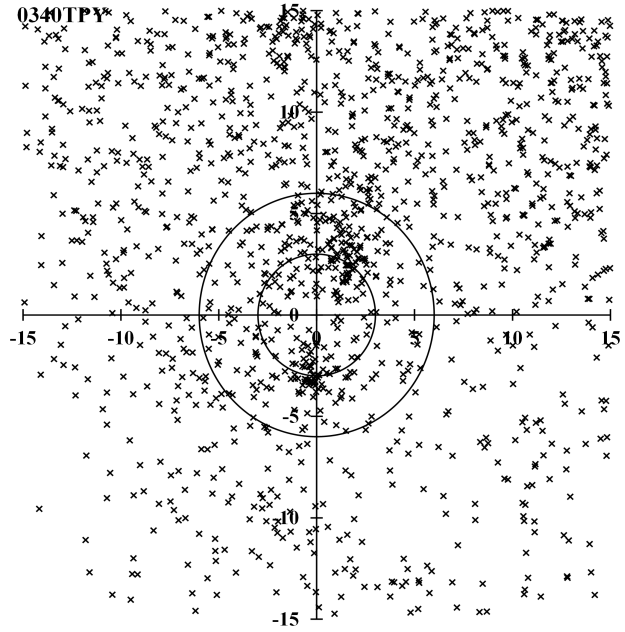

b.)

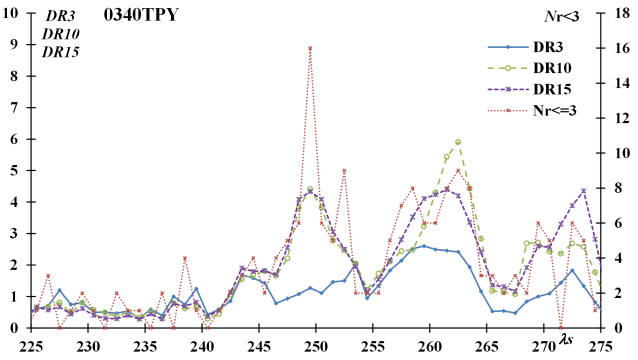

Figure 1 – a.) Radiant distribution of #0340 TPY centered at $(\lambda - \lambda_\odot, \beta) = (261.2, -36.3)$ for the period of $\lambda_\odot = 248$–268. b.) Activity profile based on the inner circle in Figure 1a. $Nr <= 3$ is the number of meteors within 3 degrees from the center (the inner circle) and DRs are the density ratios of radiants for details see Koseki (2019).

3.2 September Lyncids

The book that is the prototype for the SD states #81 SLY as Table 5 (Jenniskens, 2006).

A meteor shower was identified based on a small number of photographic meteors at that time, so there were large variations. After that, SLY0 was posted as a reference, and it has been in its current form since 2015.

Table 4 – #0340 TPY in the SD. See the text for the abbreviations.

CODE	s	Ra	De	Vg	LoS	S_LoR	LaR	References
0340TPY00	0	139.0	−25.5	60.1	249.4	261.96	−39.09	1) SonotaCo, 2009
0340TPY01	0	151.4	−24.4	62.3	264	259.58	−33.53	2) Jenniskens et al., 2016
0340TPY02	0	151.4	−24.4	63.2	264	259.58	−33.53	3) Jenniskens et al., 2016

Table 5 – Prototype of #0081 SLY (Jenniskens, 2006). N is the number used to determine the data.

Code	Name	Dates (2000)		Peak	λ_{max}				
#81 SLY	Sep. Lyncids	09/26–09/29		Sep. 28	185.0				
N	a	q	i	ω	Node	R.A.	Decl.	Vg	Reference
1	9.05	0.880	138.0	221.9	187.0	81.2	+46.6	65.2	PK#572513
2	76.970	0.770	136.5	152.5	185.9	110.9	+47.9	65.0	L71B

PK – V. Porubčan and L. Kornoš, The Taurid meteor shower. ESA SP 500 (2002), 177–180.
L71B – B.A. Lindblad, 2. A computerized stream search among 2401 photographic meteor orbits. Smithsonian Contrib. Astrophys. 12 (1971), 14–24.

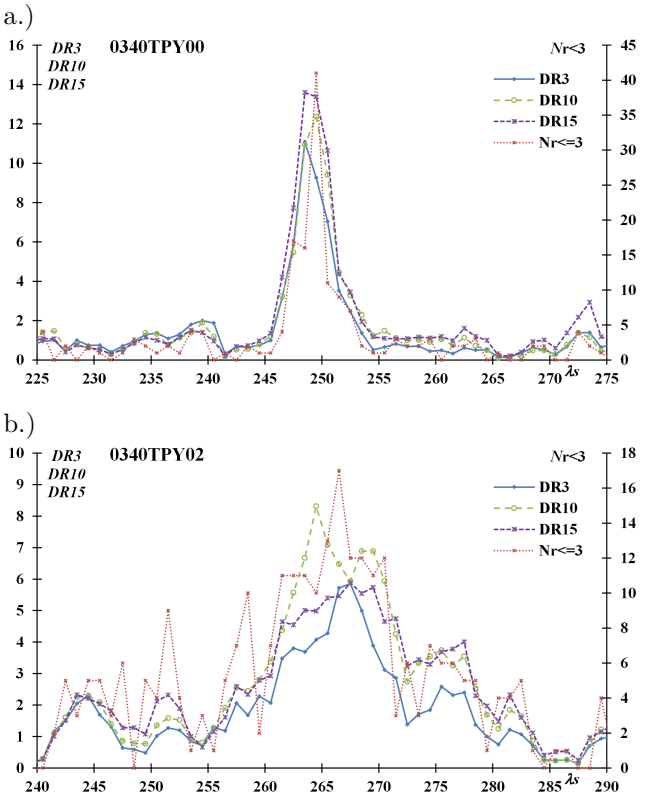

Figure 2 – a.) Activity profile of #0340TPY00 $(\lambda-\lambda_\odot, \beta) = (261.96, -39.09)$. b.) Activity profile of #0340TPY02 $(\lambda - \lambda_\odot, \beta) = (259.58, -33.53)$.

Figure 3 shows the radiant distribution centered at $(\lambda - \lambda_\odot, \beta) = (287, 29)$ for the period of $\lambda_\odot = 167$–187. The concentration upper left is SLY00 and the lower right is SLY01. An open circle near SLY01 is formerly included in Jenniskens' SLY in the second line; this shower was named simply 'Lyncids' by Lindblad.

Figures 4a and 4b are redrawn activity profiles of SLY00 and SLY01 by counting the radiant number around each exact position shown in Table 6. SLY02 existed in the SD version of 2018 January 18 but was removed for the reason described in Section "2.2 Streams removed from the Working list", though it might be a confirmation of SLY00.

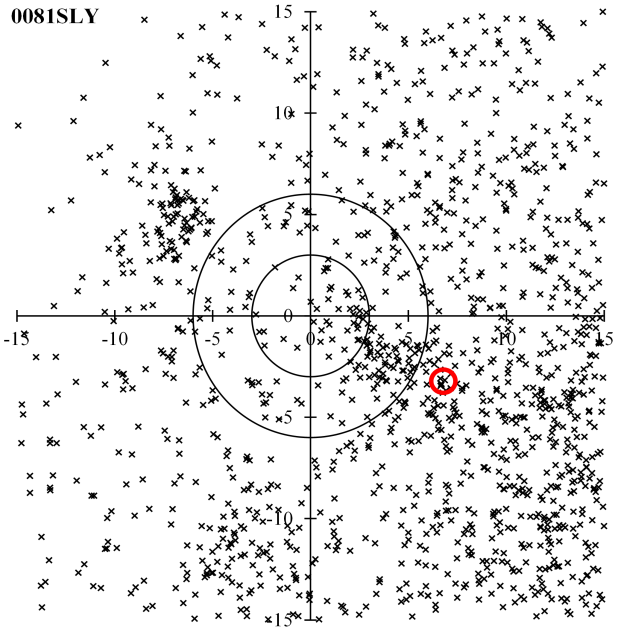

Figure 3 – Radiant distribution of #0081 SLY centered at $(\lambda - \lambda_\odot, \beta) = (287, 29)$ for the period of $\lambda_\odot = 167$–187. An open circle is Lindblad's Lyncids.

It turns out that these two are completely different activities. SLY00 should be qualified as the established shower, though SLY01 is surrounded by active sporadic background and might be not enough to be established. In any case, appropriate numbers and names should be given to each.

3.3 Microscopiids / Southern June Aquilids

#0165 SZC is now classified as an established one but this is not good. #0165 SZC is described as 'simply equals to alpha Microscopiids' in Jenniskens's list (Jenniskens, 2006) and this is quite suggestive. Observations of CMOR[a] confirmed the activity of SZC. It should be noted that the observations so far have been made by radar.

[a]Radar Meteor Radiants (CMOR): `https://fireballs.ndc.nasa.gov/cmor-radiants/`

Table 6 – #0081 SLY in the current SD.

CODE	s	Ra	De	Vg	LoS	S_LoR	LaR	References
0081SLY00	0	107.4	55.0	59.97	167	294.70	32.27	1) Molau & Rendtel, 2009
0081SLY01	0	110.2	48.4	66.77	186	278.78	25.99	2) Molau & Rendtel, 2009

Table 7 – #0165 SZC and #0370 MIC in the SD with the related #0295 JAQ by the remarks.

CODE	s	Ra	De	Vg	LoS	S_LoR	LaR	Remarks	Ote	References
0165SZC00	1	304.80	−33.92	33.17	79.70	219.50	−13.94	*A,*B	R	1) Gartrell & Elford, 1975
0165SZC01	1	304.7	−32.8	38.6	80.5	218.89	−12.83	*A	R	2) Brown et al., 2008
0165SZC02	1	319.3	−27.6	39.2	104	209.24	−11.26	*A	T	3) Jenniskens et al., 2016
0165SZC04	1	320.4	−26.5	39.9	106.5	208.03	−10.51		T	5) Shiba, 2022
0295JAQ00	−2							*C		1) Jenniskens, 2006
0370MIC00	0	320.3	−28.3	38	104	209.87	−12.20		R	1) Brown et al., 2010

*A: Member of 295/JAQ Complex
*B: In Gartrell & Elford 1975, the shower has a code 6.08 (Table 1)
*C: June Aquilid Complex, Group members: 164/NZC, 165/SZC; removed, empty record

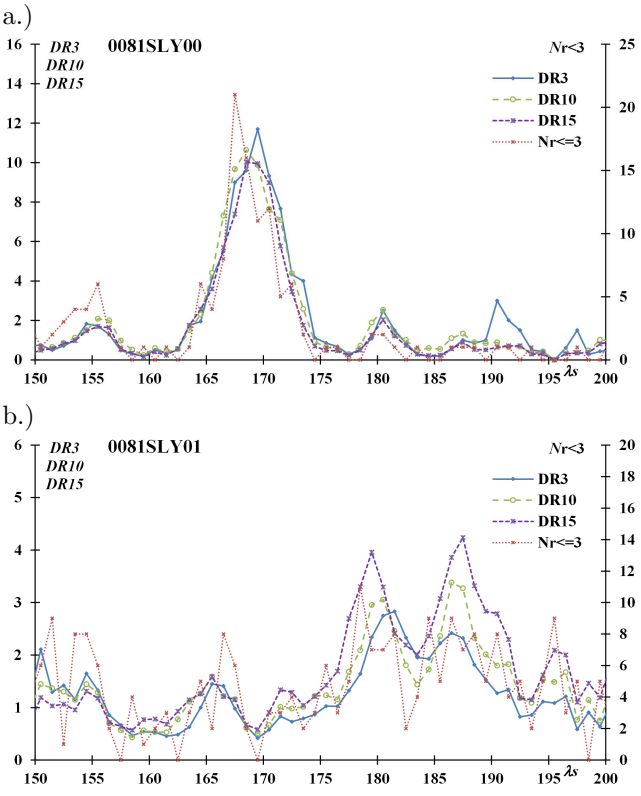

Figure 4 – a.) Activity profile of 0081SLY00 $(\lambda - \lambda_\odot, \beta) = (294.70, 32.27)$. b.) Activity profile of 0081SLY01 $(\lambda - \lambda_\odot, \beta) = (278.78, 25.99)$.

Classification of Jenniskens et al.'s video observations as SZC is where the error began (Table 7). Their observations should have been #0370 MIC instead of #0165 SZC. The original SZC, radar shower, is active more than half a month earlier than the video SZC (Table 7) and very difficult target for video observations (Figure 5a). The misidentified SZC, video shower, catches MIC activity (Figure 5b), and its activity profile shows the earliest activity begins considerably later than the radar SZC (Figure 5c).

It is very natural that the radiant distribution and the activity profile drawn by using #0370 MIC00 data will be almost the same as the figures based on #0165SZC04. Figures 6a and 6b give the detail.

It is clear that SZC02 and SZC04 must be removed from #0165 SZC and moved to #0370 MIC. Moreover, the relationship to #0295 JAQ that should be deleted is described for SZC0 to SZC2. Of course, the MDC must deal with this, but on the other hand, those who report observations to the MDC must also strictly distinguish between #0165 SZC and #0370 MIC.

3.4 phi-Piscids

The errors in the previous three cases were clear, but #0382 PPS is more difficult to judge, though #0382 PPS is classified as established. The first report of #0372 PPS is based on CMOR observations, but as shown in Figure 7, the activity is obscured by the background and is not clear. Figure 7 shows the radiant distribution recorded by CMOR from 2018 to 2022 (left to right) at the supposed maximum $\lambda_\odot = 106$. #0382 PPS is only marked in 2018 though is recorded also in 2019 at $\lambda_\odot = 104$. #0382 PPS might only stand out sometimes from Apex activity and may not recognize every year by radar observations.

The difference in the solar longitude at the maximum seems to be large for the established shower, suggesting that #0372 PPS might have two different activities. Figures 8a and 8b show the result of examining the radiant distribution by dividing it into two as shown in Table 9; the range has a width of 10 on both sides of 90 and 110 with 100 as the boundary, and the cen-

Table 8 – #0372 PPS in the SD.

CODE	s	Ra	De	Vg	LoS	S_LoR	LaR	Ote	References
0372PPS00	1	20.1	24.1	62.9	106	281.71	14.47	R	1) Brown et al., 2010
0372PPS01	1	12.9	22.0	67.1	94.0	286.56	15.15	T	2) Holman & Jenniskens 2013
0372PPS02	1	17.0	25.0	66.5	103	282.38	16.40	T	3) Jenniskens et al., 2016

a.)

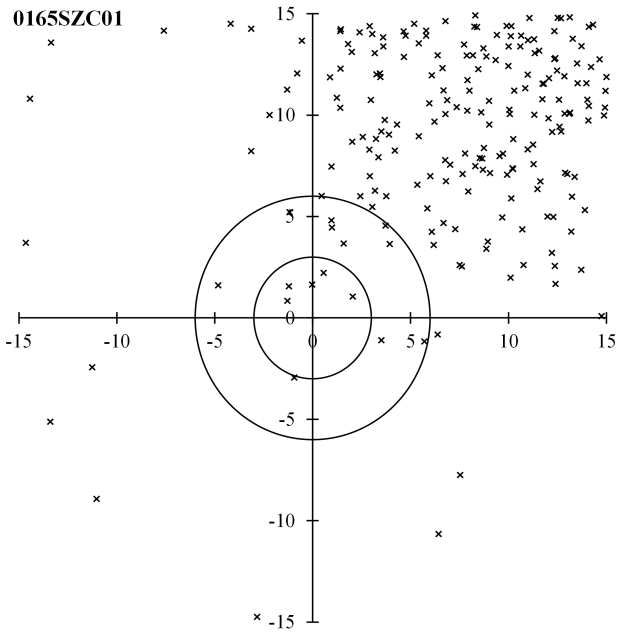

b.)

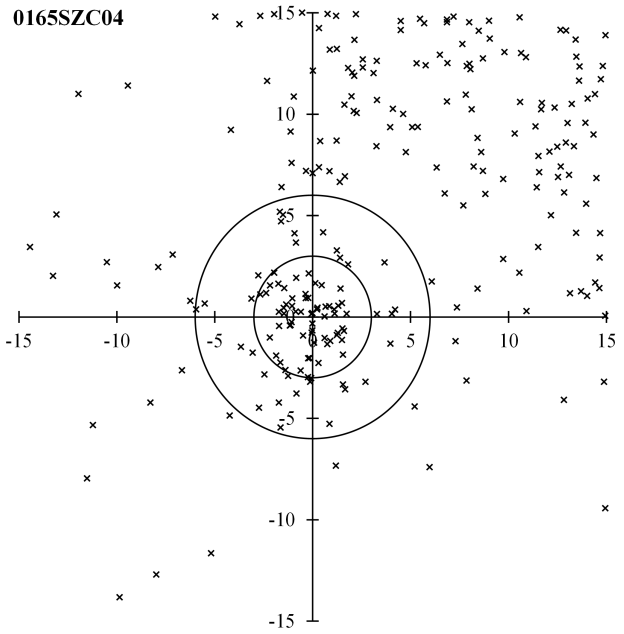

c.)

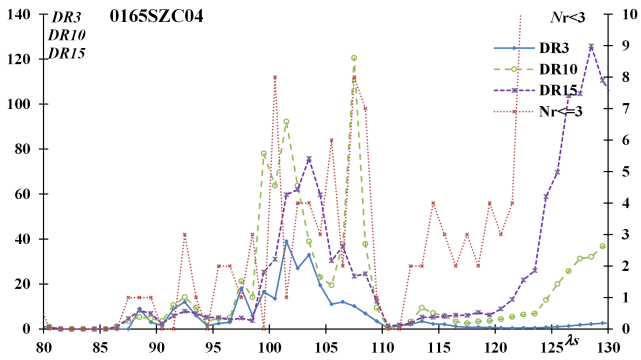

Figure 5 – a.) Radiant distribution of #0165SZC01 centered at $(\lambda - \lambda_\odot, \beta) = (218.89, -12.83)$ for the period of $\lambda_\odot = 70.5$–90.5. b.) Radiant distribution of #0165SZC04 centered at $(\lambda - \lambda_\odot, \beta) = (208.0, -10.5)$ for the period of $\lambda_\odot = 96.5$–116.5. c.) Activity profile of #0165SZC04.

a.)

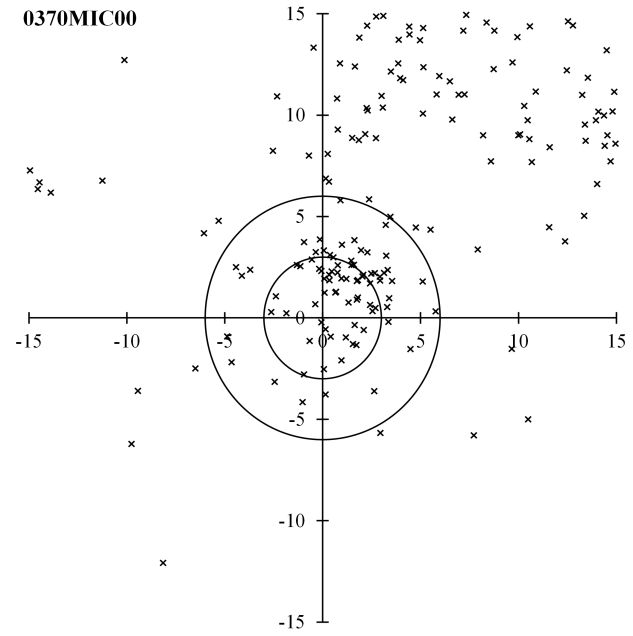

b.)

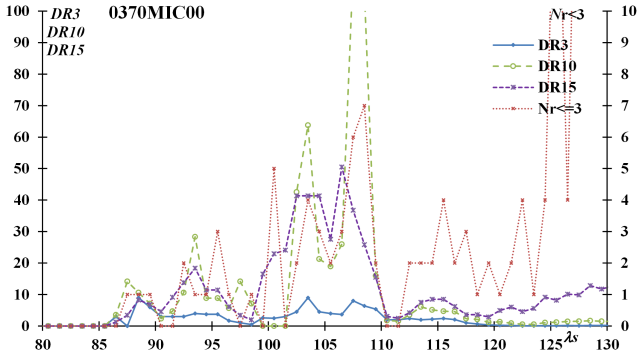

Figure 6 – a.) Radiant distribution of #0370MIC00 centered at $(\lambda - \lambda_\odot, \beta) = (209.87, -12.20)$ for the period of $\lambda_\odot = 94$–114. b.) Activity profile of #0370MIC00.

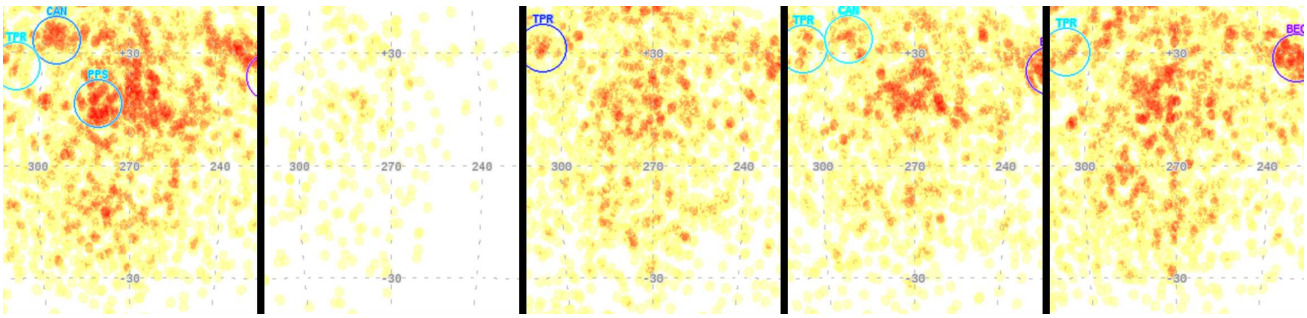

Figure 7 – Radiant distribution of #0372 PPS recorded by CMOR from 2018 to 2022 (left to right) at the supposed maximum $\lambda_\odot = 106$: the reversed figures from originals.

a.)

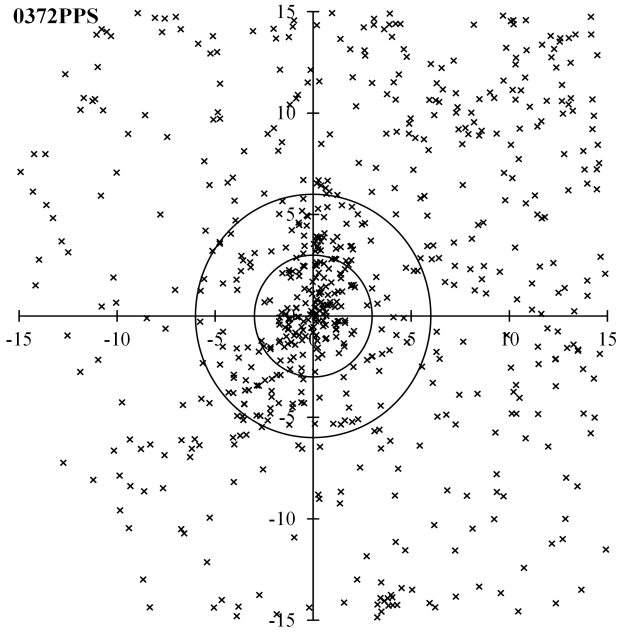

b.)

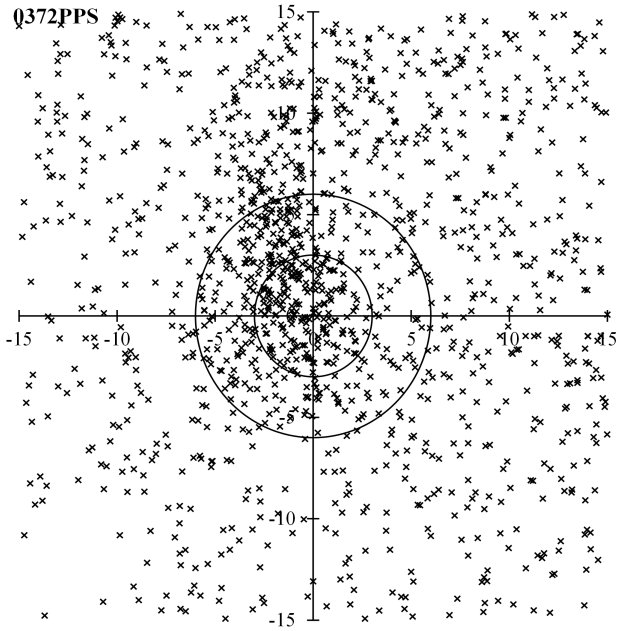

Figure 8 – a.) Radiant distribution of #0372PPS_A centered at $(\lambda - \lambda_\odot, \beta) = (284, 15)$ for the period of $\lambda_\odot = 80$–100. b.) Radiant distribution of #0372PPS_B centered at $(\lambda - \lambda_\odot, \beta) = (280, 16)$ for the period of $\lambda_\odot = 100$–120.

a.)

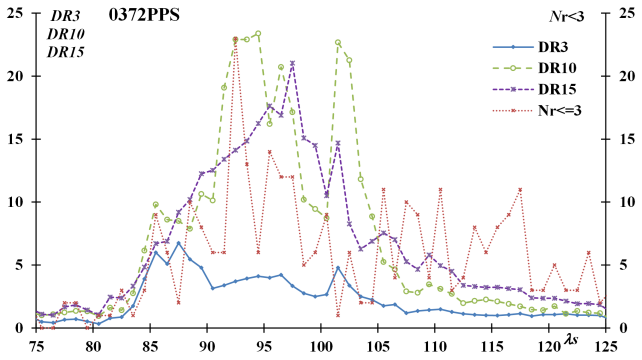

b.)

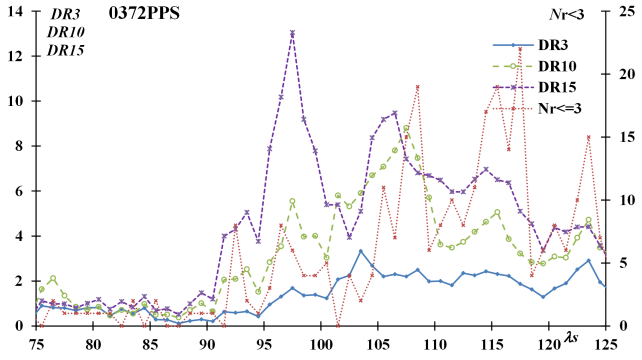

Figure 9 – a.) Probable activity profile of #0372PPS_A; no correction for the radiant drift. b.) Probable activity profile of #0372PPS_B; no correction for the radiant drift.

ter position is changed according to each distribution. The distribution appears to be upward-sloping in the first half and downward-sloping in the second half. I won't go into detail here, but the least square analysis shows that the radiant moves in that direction in their respective ranges.

The meteor numbers within the inner circle ($r < 3$) are 147 and 192 for the earlier range and the latter respectively. The activity profiles based on that number are shown in Figures 9a and 9b; it is necessary to note that they are simple rates not correcting for the radiant drift. These figures suggest that #0372 PPS has two activities though not so clear because #0372 PPS locates in the midst of the apex meteor activity. We should be careful to study meteor activities that are surrounded by active sporadic backgrounds whether they are the established ones or not.

4 Discussions

Although the SD has improved, there are still many things that have been identified as the same or different due to incorrect identifications. theta-Pyxidids (#0340 TPY) consists of two activities, September Lyncids (#0081 SLY) also, Microscopiids (#0370 MIC) and Southern June Aquilids (#0165 SZC) are confused cases, and phi-Piscids (#0372 PPS) shows how difficult identification can be when there is high peripheral activity. These are the typical examples only and there are many similar cases in the SD.

These are partly due to the lack of materials at the time of the study, but also due to insufficient understanding or carelessness of the authors and reviewers. Basically, the MDC does not have the authority to overturn the author's judgment at the time of registration. Hajduková (2023) states on this matter:

> We would like to emphasize here that it is not the task of database operators to decide whether a newly submitted stream is a duplicate of a stream already present in the MDC. It is the responsibility of the reviewer of the publication describing the new shower discovery, or anyone who undertook such evaluation and published it in a peer-reviewed scientific journal or one of the amateur journals: the WGN (Journal of the IMO) or Meteor News.

Table 9 – Possible division of #0372 PPS.

	$\lambda_\odot$	$\lambda - \lambda_\odot$	β	r	$\Delta\lambda_\odot$	N
PPS_A	90	284	15	3	10	147
PPS_B	110	280	16	3	10	192

We must be aware that SD contains erroneous data, and at the same time, we must be careful not to amplify errors. Submissions from papers published in WGN will be accepted at MDC as is. It should be examined to see if it has already been reported, and not to apply for each data resulting from radiant drift by each period or subgroup under examination.

References

Hajduková M., Rudawska R., Jopek T., Koseki M., Kokhirova G., and Neslušan L. (2023). "Modification of the Shower Database of the IAU Meteor Data Center". *Astronomy and Astrophysics*, **671**, A155. doi:10.1051/0004-6361/202244964.

Jenniskens P. (2006). *Meteor Showers and their parent comets*. Cambridge. Table 7, 'Working list of cometary meteor showers', 691-746. (http://www.astro.sk/~ne/IAUMDC/STREAMLIST/meteoroidstreamworkinglist.pdf).

Jopek T. J., Hajduková M., Rudawska R., Koseki M., Kokhirova G., and Neslušan L. (2023). "New nomenclature rules for meteor showers adopted". *New Astronomy Reviews*, **96**, 101671. doi:10.1016/j.newar.2022.101671.

Koseki M. (2016). "Research on the IAU meteor shower database". *WGN, the Journal of the IMO*, **44:5**, 151–169.

Koseki M. (2019). "Profiles of meteor shower activities inferred from the radiant Density Ratios (DR)". *WGN, Journal of the IMO*, **47:6**, 168–179.

SonotaCo (2009). "A meteor shower catalog based on video observations in 2007–2008". *WGN, Journal of the IMO*, **37:2**, 55–62. See also "SonotaCo Network Simultaneously Observed Meteor Data Sets", http://sonotaco.jp/doc/SNM/.

Handling Editor: Javor Kac

Preliminary results

Result of the IMO Video Meteor Network – First Quarter 2020

Sirko Molau[1], *Stefano Crivello, Rui Goncalves, Carlos Saraiva, Enrico Stomeo, Jörg Strunk, and Javor Kac*

The IMO Video Meteor Network cameras recorded nearly 38 000 meteors in over 12 000 observing hours during 2020 January, more than 21 000 meteors in nearly 10 000 observing hours during 2020 February, and more than 22 000 meteors in almost 12 000 observing hours during 2020 March. Flux density and population index profiles are presented for the Quadrantids. A method is discussed for correcting the flux density for the Moon influence, on the case of Antihelion meteors.

Received 2023 June 5

1 Introduction

In the first quarter of 2020, little more than 80 video cameras were in operation in the IMO Video Meteor Network. The weather was not particularly good as is typical for this time of year, but we still could collect a considerable data set of winter meteor activity (Figure 1).

In January, we recorded nearly 38 000 meteors in over 12 000 observing hours. That is 150 hours and 4 000 meteors more than in 2017, which had been best January so far (Molau et al., 2017). With nearly 10 000 observing hours and 21 000 meteors, February's totals were well below the previous year, but still one of the best February outputs in the history of the IMO network. The same holds for March, where we recorded over 22 000 meteors in more than 11 700 observing hours. In total, the first quarters of 2019 and 2020 delivered almost the same result, with 2020 being marginally 200 observing hours and 100 meteors ahead.

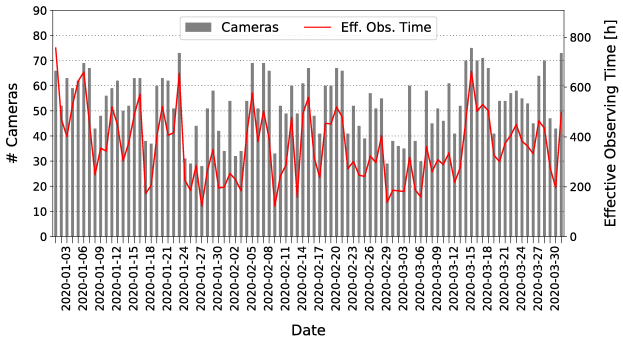

Figure 1 – Number of active cameras per night (grey bars) and effective observing time of these cameras (red line) in the first quarter of 2020.

Whereas the hourly meteor count rose briefly during the Quadrantids, it declined noticeably thereafter and reached the annual low of about two meteors per hours in March (Figure 2).

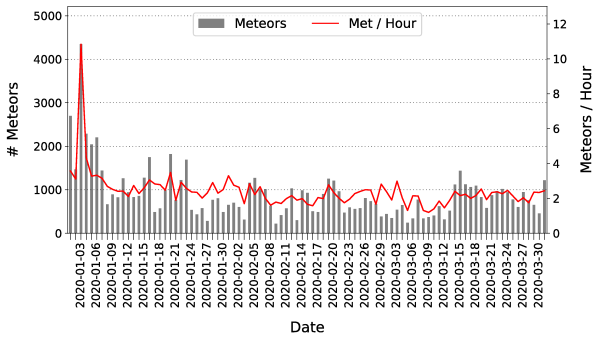

Figure 2 – Number of recorded meteors per night (grey bars) and average number of meteors per hours (red line) in the first quarter of 2020.

2 Quadrantids

Which brings us directly to the only highlight of the review period. The radiant of the Quadrantids only rises to substantial heights after local midnight, and hence the waxing moon did not interfere in the more significant second half of night. The peak was, however, predicted for 8 UT on January 4, well beyond the European observing window. Hence, the hourly rates were expected to increase steeply in the morning hours of January 4, when both the shower activity and the radiant altitude were rising. On the other hand, the show should have been over by the next evening, when the steeply falling rates would coincide with a radiant at lower culmination. And that was what we observed. Whereas in the first hour after midnight of January 3/4

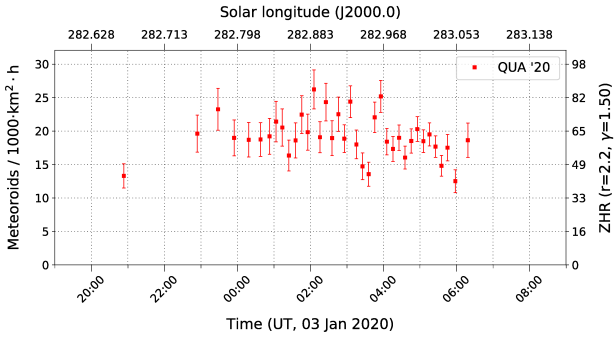

Figure 3 – Flux density of the Quadrantids on 2020 January 3/4, derived from observations of the IMO Network.

[1]Abenstalstr. 13b, 84072 Seysdorf, Germany.
Email: sirko@molau.de

IMO bibcode WGN-513-molau-2020q1
NASA-ADS bibcode 2023JIMO...51...63M

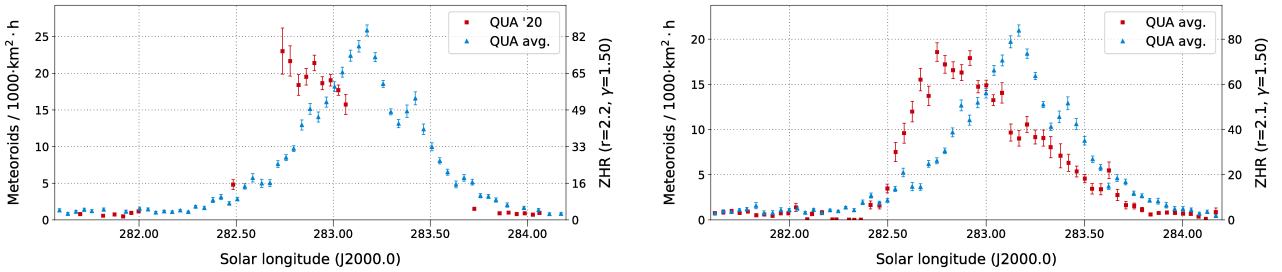

Figure 5 – Comparison of the activity profile of the Quadrantids 2020 with the average of the years 2011 and 2019 (left). On the right side, the 2020 profile was augmented with the already available data of 2021 to 2023.

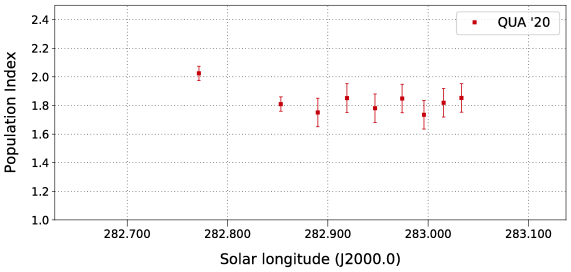

Figure 4 – Population index of the Quadrantids in January 2020.

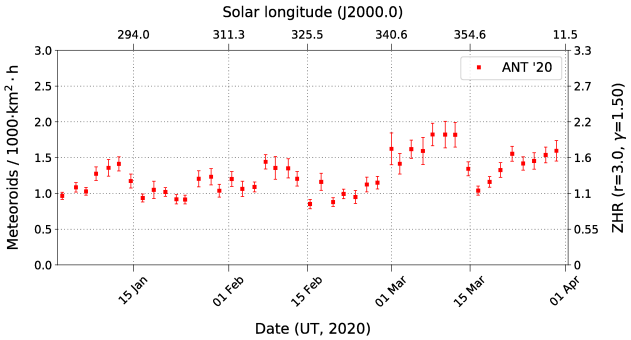

Figure 6 – Activity profile of the Antihelion source in the first quarter of 2020, derived from observations of the IMO Network.

we recorded about 100 Quadrantids, it was 700 in the last hour before dawn. On the next evening, the rate had declined to about 10 Quadrantids per hour.

If the meteor counts are corrected for the radiant altitude and other relevant parameters, we obtain a nearly constant flux density of about 20 meteoroids per 1 000 km^2 an hour for the morning of January 4, with even a decreasing trend towards dawn (Figure 3). This implies that the 2020 Quadrantid peak must have been a few hours early.

The population index was near $r = 1.8$ throughout the whole night (Figure 4).

The early maximum is confirmed if we compare the activity profile of 2020 with the long-term average of the years 2011 to 2019 (Figure 5, left). It becomes even more obvious if we add the so far incomplete data sets of 2021 to 2023 (Figure 5, right). It seems that starting from 2020 the Quadrantid peak has suddenly shifted backward by 0.°4 solar longitude, or 10 hours in time. The visual observations of IMO yield a Quadrantid peak in 2020 at 4 UT (International Meteor Organization, 2020), i.e., also earlier than predicted, but not by so much.

3 Other meteor showers

And that was about it for meteor shower activity in the first quarter of 2020. Neither the delta Leonids nor any other shower was clearly visible in our data. The flux density of the Antihelion source was less than 1.5 meteoroids per 1 000 km^2 an hour in January and February, and reached values above 1.5 in March (Figure 6). The peaks correlate "expectedly" with the times of full moon, which occurred the first third of each month.

4 Correcting the flux density for the influence of the Moon

At IMC 2022 a method to reduce the impact of moon was presented. The flux database was enriched by the Sun's depression, Moon's altitude and phase, and the distance of the Moon from the field of view. If observations with significant moon disturbance (moon phase $> 10\%$, moon altitude $> 0°$, and moon distance $< 90°$) are left out, the periodic variations get somewhat smaller (Figure 7). The result is still not satisfactory, because a significant fraction of observations are omitted and the error bars are getting correspondingly larger.

It would be better if we could correct the flux density for the influence of the Moon. The relevant parameters are available now – it just needs the right correction

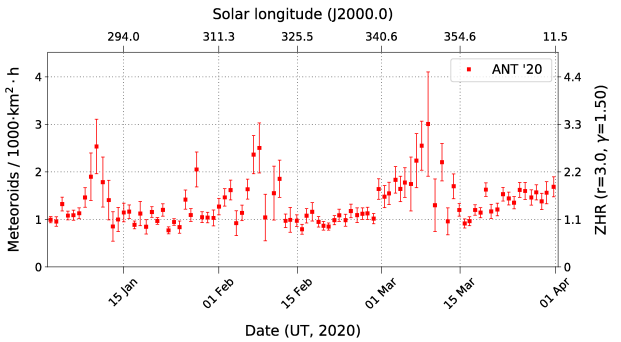

Figure 7 – Activity profile of the Antihelion source in the first quarter of 2020, whereby observations with significant moon disturbance were omitted.

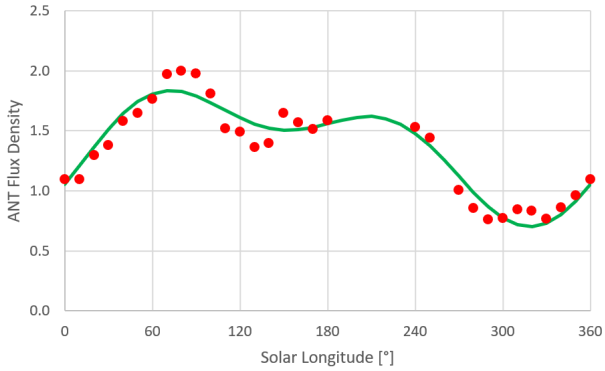

Figure 8 – Average Antihelion activity profile of the years 2011 to 2019, and a fit from the sum of two sine functions.

function. In the following we will describe how to derive such a correction function.

To start, we need a reliable "calibration standard", i.e., a shower with constant activity and long activity interval. The Antihelion source is the first choice, but is its activity really constant over the year? To determine that, we computed the average Antihelion activity profile for the years 2011 to 2019. Over that long time span, the impact of Moon should approximately level out. We obtained a profile, that can be approximated by a sum of two sine functions (Figure 8).

The dependency of the flux density FD of the Antihelion source from the solar longitude SL (in degree) can be approximated by:

$$FD = 1.38 + 0.42\sin(SL - 37) + 0.27\sin(2SL - 16) \quad (1)$$

Next, we accumulated all flux density measures of the Antihelion source depending on the corresponding Moon parameter, and corrected for the expected values at the corresponding solar longitude according to Equation 1. We only used observations where the Moon was above the horizon.

In a first test series, we determined the dependency of the Antihelion flux density from the three parameters Moon phase, Moon altitude and Moon distance (from the center of field of view) independently, and fitted a quadratic function with three free parameters each.

Interestingly, the correction for the Moon phase was not a monotonic function. The smallest correction was

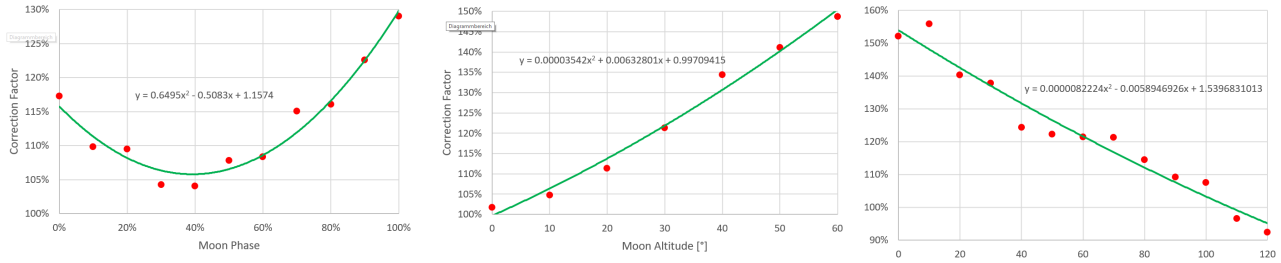

Figure 9 – Impact of the Moon phase (left), Moon altitude (center) and Moon distance from the field of view (right) on the normalized flux density profile of the Antihelion source.

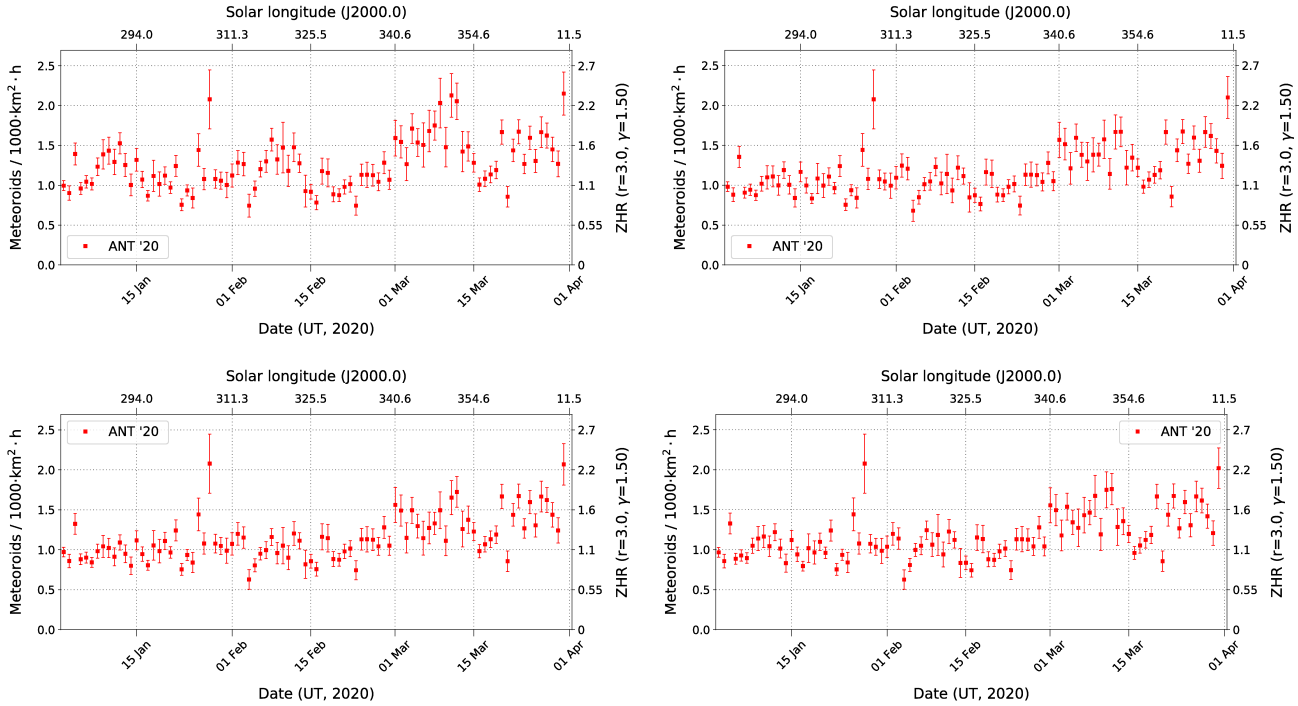

Figure 10 – Uncorrected activity profile of the Antihelion source in the first quarter of 2020 (upper left) and profiles that were corrected for the moon phase (upper right), moon altitude (lower left), and moon distance (lower right).

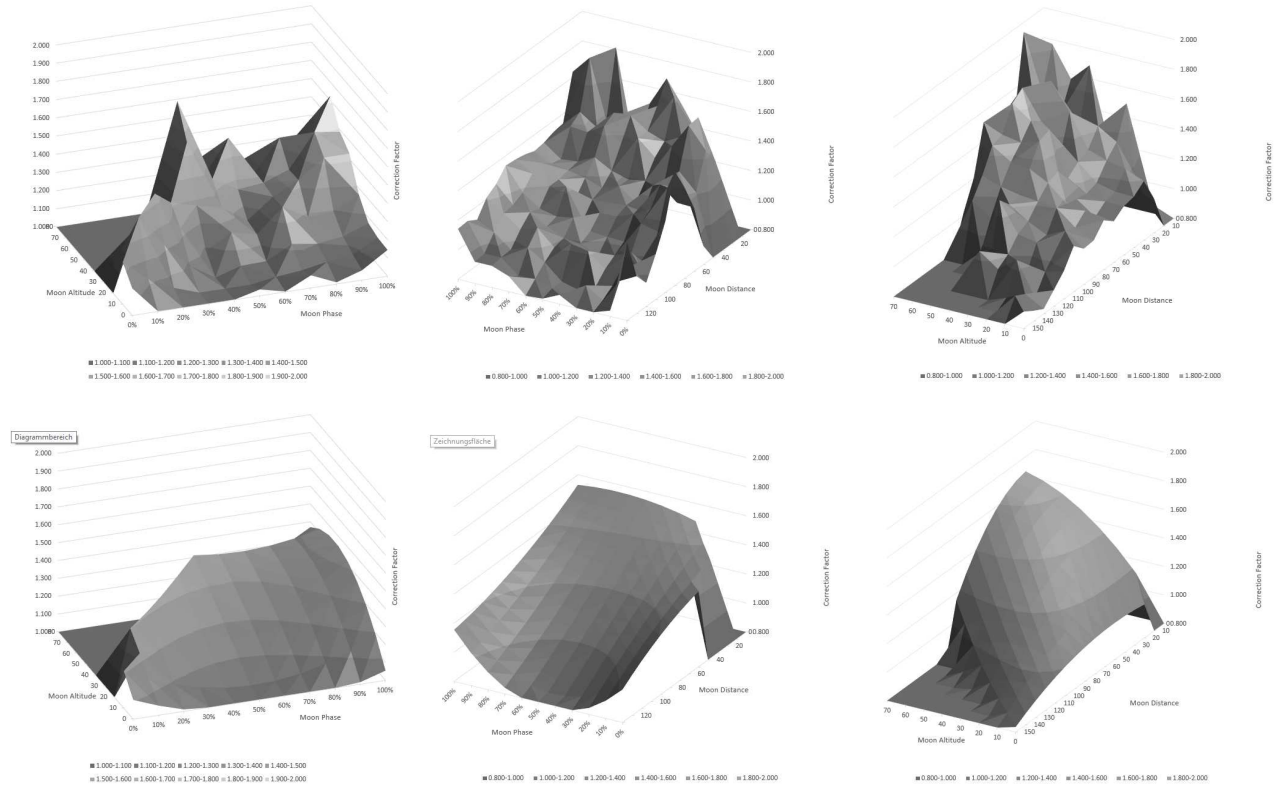

Figure 11 – Impact of the Moon phase and altitude (left), Moon phase and distance (center) and Moon altitude and distance (right) on the normalized flux density profile of the Antihelion source. The upper row shows the original measures, the lower row the quadratic fit.

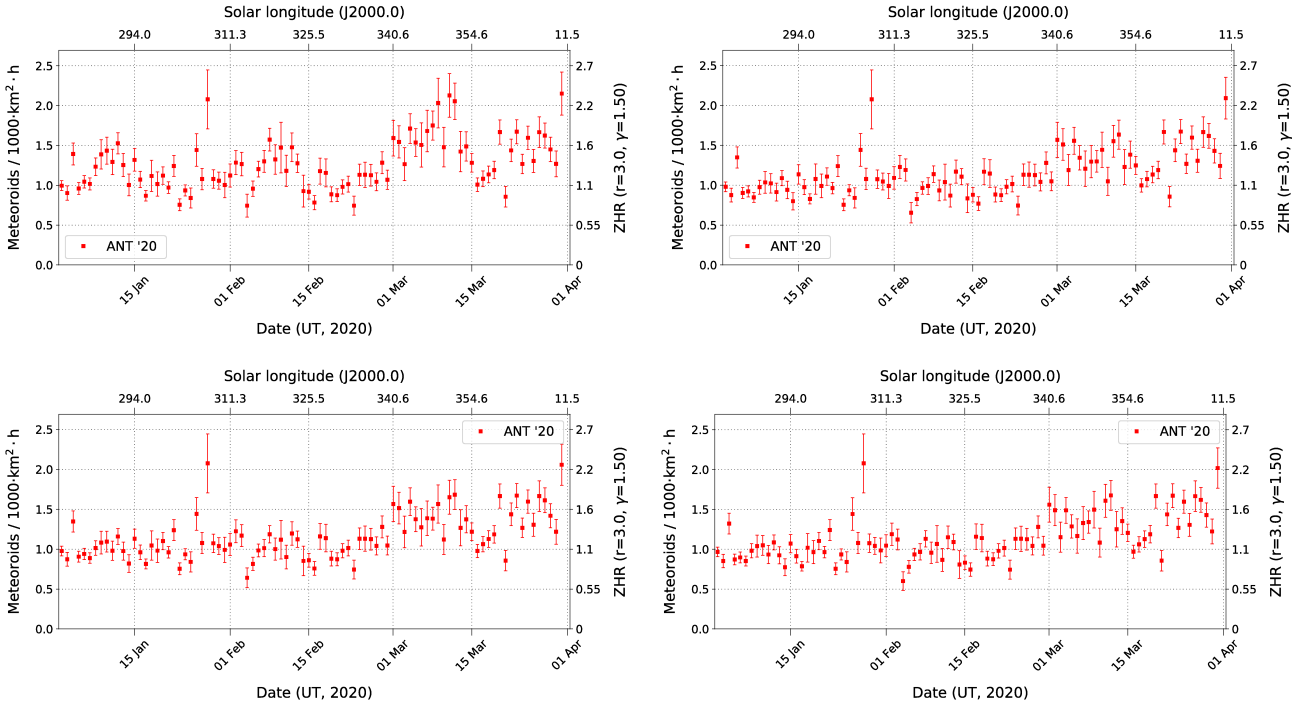

Figure 12 – Uncorrected activity profile of the Antihelion source in the first quarter of 2020 (upper left) and profiles that were corrected for the Moon phase and altitude (upper right), Moon phase and distance (lower left), and Moon altitude and distance (lower right).

obtained for a Moon phase of about 40%. For smaller or larger Moon phases, the ANT flux density deviated stronger from the average (Figure 9, left). The disadvantage of that modeling is, that the correction remains nearly constant during the night, whereas the impact of the Moon on the field of view of the camera is highly variable.

For the dependency of the flux density on the Moon's altitude we got a nearly linear function (Figure 9, center). The higher the Moon, the larger the correction

factor. That is not unexpected, but the Moon altitude says little about the brightness or distance of the Moon.

The correction factor depends also near linearly on the Moon's distance (Figure 9, right). The farther the Moon is away from the field of view, the smaller is the deviation in flux density. The brightness of the Moon is neglected in this case, however.

In Figure 10 we show the effect of the quadratic correction functions on the activity profile of the Antihelion source in the first quarter of 2020. The periodic variations are getting smaller in all three cases, but do not disappear completely. All methods perform about equally well, but the Moon altitude correction may be subjectively a little better.

Since each parameter alone does not reflect the Moon influence completely as described, we started a second test series where we combined two of these three parameters at a time. The quadratic regression now has nine free parameters and since there are many more parameter combinations, we have fewer observations for each of these. Hence, we see larger scatter in the data. Figure 11 shows in the upper row the original measures and in the lower row the quadratic fit for a combination of the Moon phase and altitude (left), Moon phase and distance (center) and Moon altitude and distance (right), respectively. It can be seen that certain parameter combinations cannot occur in the night sky (e.g., a thin crescent near zenith).

Finally, Figure 12 shows that the application of these quadratic correction functions further smoothes the activity profile. Again, all the parameter combinations perform equally well, so that there is not one which can be particularly recommended. The periodic variations are nearly gone and the expected rise in Antihelion activity toward the end of the first quarter (cf. Figure 8) is getting more prominent.

A combination of all three parameters was also tested, but did not yield further improvements. The number of free parameters in the quadratic fit further increases to twenty-seven, and once more there is significantly less data per parameter combination. In addition, this model has more redundancies. The Moon altitude is always low for small Moon phases, for example, since the Moon is either setting shortly after the Sun, or rising shortly before it. For the same reason, we see smaller Moon distances from the field of view when the Moon phase is increasing, and the Moon distance is on average smaller for middle Moon altitudes, because the cameras are typically not pointed to the horizon or zenith.

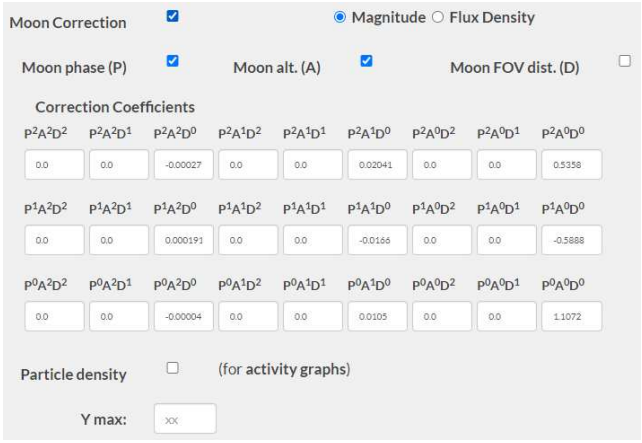

Figure 13 – Implementation of the different correction functions in Meteorflux.

All correction options were implemented in MeteorFlux (Figure 13), whereby you can select both the parameter combination and the coefficients of the correction function. We will see in the future whether the correction for the Moon influence yields the same improvement for showers other than the Antihelion source.

References

International Meteor Organization (2020). "Quadrantids 2020 campaign". `https://www.imo.net/members/imo_live_shower/?shower=QUA&year=2020` .

Molau S., Crivello S., Goncalves R., Saraiva C., Stomeo E., and Kac J. (2017). "Results of the IMO Video Meteor Network – January 2017". *WGN, Journal of the IMO*, **45:3**, 63–66.

Handling Editor: Javor Kac

Table 1 – Observational statistics for the first quarter of 2020.

Code	Name	Place	Camera	October			November			December		
				Nights	Time [h]	Meteors	Nights	Time [h]	Meteors	Nights	Time [h]	Meteors
ARLRA	Arlt	Ludwigsfelde/DE	LUDWIG2	21	134.9	700	21	86.7	261	27	169.5	646
BERER	Berkó	Ludanyhalaszi/HU	HULUD1	4	38.7	152	—	—	—	—	—	—
BIATO	Bianchi	Mt. San Lorenzo/IT	OMSL1	25	183.7	474	24	201.6	361	22	94.1	169
BOMMA	Bombardini	Faenza/IT	MARIO	26	217.4	691	26	212.9	554	26	170.8	419
BRIBE	Klemt	Herne/DE	HERMINE	19	118.9	288	19	70.4	101	23	147.0	292
		Berg. Gladbach/DE	KLEMOI	21	101.3	241	16	66.2	101	21	141.8	271
CARMA	Carli	Monte Baldo/IT	BMH2	24	274.7	1333	25	258.7	922	20	153.5	534
CASFL	Castellani	Monte Baldo/IT	BMH1	24	261.1	1298	25	262.6	1046	20	151.3	556
CINFR	Cineglosso	Faenza/IT	JENNI	28	225.8	692	26	219.2	611	26	181.9	373
CRIST	Crivello	Valbrevenna/IT	ARCI	23	203.6	621	23	195.1	331	24	138.8	263
			BILBO	23	204.1	897	23	191.5	475	25	163.0	322
			C3P8	20	179.0	407	19	163.5	237	23	162.1	215
			STG38	23	220.9	1060	23	205.5	617	22	169.7	471
ELTMA	Eltri	Venezia/IT	MET38	10	92.9	218	16	139.6	264	19	106.1	180
FORKE	Förster	Carlsfeld/DE	AKM3	15	131.3	374	7	30.0	58	21	161.5	354
GONRU	Goncalves	Tomar/PT	TEMPLAR1	24	156.2	404	26	202.8	462	25	180.0	310
			TEMPLAR2	21	163.4	352	25	204.5	374	24	174.5	259
			TEMPLAR3	16	128.9	112	18	163.7	81	20	146.3	63
			TEMPLAR4	23	141.9	312	23	171.3	274	23	148.8	231
			TEMPLAR5	20	137.4	344	23	176.0	297	22	137.6	157
GOVMI	Govedič	Središče ob Dr./SI	ORION2	23	122.6	409	23	151.8	255	19	134.6	305
			ORION3	22	160.2	206	22	175.1	154	18	117.1	113
			ORION4	20	105.7	179	23	124.6	112	14	63.7	70
HINWO	Hinz	Schwarzenberg/DE	HINWO1	22	174.8	429	16	77.1	133	23	163.8	347
IGAAN	Igaz	Budapest/HU	HUPOL	14	96.7	122	5	23.1	24	13	62.8	59
JONKA	Jonas	Budapest/HU	HUSOR	14	114.1	163	20	131.8	99	19	161.6	110
			HUSOR2	14	118.4	184	21	148.5	137	22	165.5	129
KACJA	Kac	Kamnik/SI	CVETKA	23	199.8	818	14	105.7	285	16	112.9	283
			REZIKA	23	209.7	1478	14	98.5	461	16	109.2	508
			STEFKA	23	216.5	621	14	106.5	176	15	108.7	202
		Kostanjevec/SI	METKA	23	68.4	167	24	57.0	141	19	41.1	103
KNOAN	Knöfel	Berlin/DE	ARMEFA	19	132.2	224	14	57.2	69	24	172.8	256
KOSDE	Koschny	La Palma/ES	ICC7	17	96.2	153	16	69.1	83	13	45.8	70
			ICC9	30	255.6	1645	28	218.7	1171	25	168.0	838
			LIC1	11	82.2	123	12	62.6	73	14	45.7	61
			LIC2	29	276.0	1860	27	216.9	1105	27	185.8	875
KWIMA	Kwinta	Krakow/PL	PAV06	11	91.5	60	9	54.9	30	19	121.6	49
			PAV07	14	118.2	106	8	43.1	34	21	139.7	77
			PAV79	15	127.1	172	11	63.4	78	22	146.2	136
LOJTO	Łojek	Grabniak/PL	PAV103	11	69.8	42	5	33.3	15	7	52.4	28
			PAV57	13	87.8	115	7	53.9	49	9	73.2	85
MACMA	Maciejewski	Chelm/PL	PAV35	16	85.9	122	12	36.7	43	20	120.2	106
			PAV36	17	127.7	169	16	77.5	84	23	165.6	161
			PAV43	16	126.5	219	14	89.9	132	26	173.3	215
			PAV60	17	136.9	241	15	94.3	144	25	179.3	266
MARRU	Marques	Lisbon/PT	CAB1	9	41.2	102	—	—	—	—	—	—
			RAN1	15	130.4	272	19	155.4	160	25	165.4	154
MISST	Missiaggia	Nove/IT	TOALDO	24	233.8	590	1	5.8	3	—	—	—
MOLSI	Molau	Seysdorf/DE	AVIS2	25	160.4	484	22	131.8	357	27	193.8	704
			DIMCAM2	25	154.5	965	23	114.5	607	25	127.6	718
			ESCIMO3	21	164.6	600	21	135.4	435	26	200.9	751
		Ketzür/DE	REMO1	24	123.9	823	25	77.1	295	26	153.9	753
			REMO2	24	151.1	716	23	85.8	239	26	182.8	582
			REMO3	25	177.5	607	25	116.9	238	27	211.8	514
			REMO4	22	163.5	727	24	106.0	277	26	196.0	680
MORJO	Morvai	Fülöpszallas/HU	HUFUL	15	131.8	137	23	167.5	118	21	166.0	95
MOSFA	Moschini	Rovereto/IT	ROVER	29	282.4	541	22	205.8	263	16	103.9	98
NAGHE	Nagy	Budapest/HU	HUKON	—	—	—	23	71.5	183	17	26.2	147
		Piszkestetö/HU	HUPIS	26	140.3	593	25	158.0	250	24	133.1	219
OTTMI	Otte	Pearl City/US	ORIE1	9	4.7	28	14	8.8	40	14	9.1	34
PERZS	Perkó	Becsehely/HU	HUBEC	16	112.1	416	12	88.9	174	8	62.3	91
SARAN	Saraiva	Carnaxide/PT	RO1	25	225.7	384	24	238.9	278	26	213.9	196
			RO2	24	163.8	411	26	226.5	361	27	180.2	232
			RO3	23	174.2	408	25	231.1	446	27	191.7	306
			RO4	24	170.0	290	24	213.9	270	19	120.3	105
SCALE	Scarpa	Alberoni/IT	LEO	22	52.1	216	16	12.3	79	21	10.2	63
SCHHA	Schremmer	Niederkrüchten/DE	DORAEMON	18	89.2	205	22	80.6	128	25	153	235
SLAST	Slavec	Ljubljana/SI	KAYAK1	23	183.6	400	13	118.4	184	18	129.6	188
			KAYAK2	24	192.3	158	16	136.2	77	17	143.1	83
STOEN	Stomeo	Scorze/IT	MIN38	28	225.2	1045	22	165.4	553	27	133.6	370
			NOA38	26	228.5	888	21	177.4	478	25	140.4	357
			SCO38	26	244.8	977	22	178.4	563	25	148.8	392
STRJO	Strunk	Herford/DE	BEMCE	19	124.4	860	25	83.9	329	22	151.8	949
			BEMCE2	—	—	—	—	—	—	3	25.1	103
			MINCAM2	17	77.4	174	21	65	88	19	102	163
			MINCAM3	12	45.6	47	14	49.9	32	21	123	246
			MINCAM4	19	112.5	297	19	59.2	79	12	71	112
			MINCAM5	19	107.4	192	16	56.6	62	17	131.3	116
TEPIS	Tepliczky	Agostyan/HU	HUAGO	9	59.5	108	2	16.8	47	—	—	—
			HUMOB	17	140.9	453	15	112.4	172	20	150.4	219
WEGWA	Wegrzyk	Nieznaszyn/PL	PAV78	22	127.3	209	14	68.3	48	21	149.3	119
YRJIL	Yrjölä	Kuusankoski/FI	FINEXCAM	14	109.4	337	11	93.2	147	15	94.9	117
ZAKJU	Zakrajšek	Petkovec/SI	PETKA	25	214.1	952	22	176.4	567	22	155.2	492
			TACKA	23	215.2	322	20	177.4	179	19	163.1	162
Sum				31	12 171.9	37 931	29	9 960.3	21 320	31	10 743.6	22 401

The International Meteor Organization

www.imo.net

Follow us on Facebook InternationalMeteorOrganization

Follow us on Twitter @IMOMeteors

Council

President: Cis Verbeeck,
Bogaertsheide 5, 2560 Kessel, Belgium.
e-mail: cis.verbeeck@gmail.com

Vice-President: Juraj Tóth,
Fac. Math., Phys. & Inf., Comenius Univ.,
Mlynska dolina, 84248 Bratislava, Slovakia.
e-mail: toth@fmph.uniba.sk

Secretary-General: Robert Lunsford,
14884 Quail Valley Way, El Cajon,
CA 92021-2227, USA. tel. +1 619 755 7791
e-mail: lunro.imo.usa@cox.net

Treasurer: Marc Gyssens, Heerbaan 74,
B-2530 Boechout, Belgium.
e-mail: marc.gyssens@uhasselt.be
BIC: GEBABEBB
IBAN: BE30 0014 7327 5911
Bank transfer costs are always at your expense.

Other Council members:
Karl Antier, 16, rue de la République,
F-04100 Manosque, France.
e-mail: karl.antier@gmx.fr
Javor Kac (see details under WGN)
Detlef Koschny, Zeestraat 46,
NL-2211 XH Noordwijkerhout, Netherlands.
e-mail: detlef.koschny@tum.de
Sirko Molau, Abenstalstraße 13b, D-84072
Seysdorf, Germany. e-mail: sirko@molau.de
Francisco Ocaña Gonzalez, C/ Arquitectura, 7.
28005 Madrid, Spain.
e-mail: francisco.ocana.gonzalez@gmail.com
Vincent Perlerin, 16, rue Georges Bernanos,
51100 Reims, France.
e-mail: vperlerin@gmail.com
Jürgen Rendtel, Eschenweg 16, D-14476
Marquardt, Germany. e-mail: jrendtel@aip.de

Commission Directors

Visual Commission: Jürgen Rendtel
Generic e-mail address: visual@imo.net
Electronic visual report form:
http://www.imo.net/visual/report/electronic
Video Commission: Sirko Molau (video@imo.net)
Photographic Commission: Bill Ward
(bill_meteor@yahoo.com)
Generic e-mail address: photo@imo.net
Radio Commission: Chris Steyaert
(radio@imo.net)
Fireball Commission: Robert Lunsford
Online fireball reports:
http://fireballs.imo.net

Webmaster

Karl Antier, e-mail: webmaster@imo.net

WGN

Editor-in-chief: Javor Kac
Na Ajdov hrib 24, SI-2310 Slovenska Bistrica,
Slovenia. e-mail: wgn@imo.net;
include METEOR in the e-mail subject line

Editorial board: Ž. Andreić, D.J. Asher,
F. Bettonvil, M. Gyssens, C. Hergenrother,
T. Heywood, J. Rendtel, C. Verbeeck,
S. de Vet, D. Vida.

IMO Sales

Available from the Treasurer or the Electronic Shop on the IMO Website	€	$
IMO membership, including subscription to WGN Vol. 51 (2023)		
Surface mail	26	30
Air Mail (outside Europe only)	49	56
Electronic subscription only	21	24
Proceedings of the International Meteor Conference on paper		
1990, 1991, 1995, 1996, 1999, 2000, 2002, 2003, per year	9	12
2007, 2010, 2011, per year	15	20
2012, 2013, 2015, 2017 per year	25	32
Proceedings of the Meteor Orbit Determination Workshop 2006	15	20
Radio Meteor School Proceedings 2005	15	20
Handbook for Meteor Observers	23	29
Meteor Shower Workbook	12	16
Electronic media		
Meteor Beliefs Project ZIP archive	6	8

Two firebals over Germany on 2023 February 26

This bright fireball appeared on 2023 February 26 at $19^{h}59^{m}47^{s}$ UTC and was captured by AllSky7 camera AMS89 Sorø (Denmark).
Copyright: Hennig Haack, AllSky7 Fireball Network.
Ten Allsky7 cameras recorded the event. Videos are available at:
`https://allsky7.net/archive.html?date=20230226&time=195947`

Another bright fireball appeared on 2023 February 26 at $20^{h}12^{m}41^{s}$ UTC and was captured by AllSky7 AMS30 Demmin (Germany).
Copyright: Wolfgang Hamburg, Michael Danielides, AllSky7 Fireball Network.
Eight Allsky7 cameras recorded the event. Videos are available at:
`https://allsky7.net/archive.html?date=20230226&time=201241`